

Alpacas in Space - An Autobiography

By

JOSEPH LEVINE
DISSERTATION

Submitted in partial satisfaction of the requirements for the degree of

DOCTOR OF PHILOSOPHY

in

Physics

in the

OFFICE OF GRADUATE STUDIES

of the

UNIVERSITY OF CALIFORNIA

DAVIS

Approved:

J. Anthony Tyson, Chair

S. Mani Tripathi

Brian Kolner

Committee in Charge

2025

Abstract

An Afghan, an Albanian, an Algerian, an American, an Andorran, an Angolan, an Antiguans, an Argentine, an Armenian, an Australian, an Austrian, an Azerbaijani, a Bahamian, a Bahraini, a Bangladeshi, a Barbadian, a Barbudans, a Batswanan, a Belarusian, a Belgian, a Belizean, a Beninese, a Bhutanese, a Bolivian, a Bosnian, a Brazilian, a Brit, a Bruneian, a Bulgarian, a Burkinabe, a Burmese, a Burundian, a Cambodian, a Cameroonian, a Canadian, a Cape Verdean, a Central African, a Chadian, a Chilean, a Chinese, a Colombian, a Comoran, a Congolese, a Costa Rican, a Croatian, a Cuban, a Cypriot, a Czech, a Dane, a Djibouti, a Dominican, a Dutchman, an East Timorese, an Ecuadorean, an Egyptian, an Emirian, an Equatorial Guinean, an Eritrean, an Estonian, an Ethiopian, a Fijian, a Filipino, a Finn, a Frenchman, a Gabonese, a Gambian, a Georgian, a German, a Ghanaian, a Greek, a Grenadian, a Guatemalan, a Guinea-Bissauan, a Guinean, a Guyanese, a Haitian, a Herzegovinian, a Honduran, a Hungarian, an I-Kiribati, an Icelander, an Indian, an Indonesian, an Iranian, an Iraqi, an Irishman, an Israeli, an Italian, an Ivorian, a Jamaican, a Japanese, a Jordanian, a Kazakhstani, a Kenyan, a Kittian and Nevisian, a Kuwaiti, a Kyrgyz, a Laotian, a Latvian, a Lebanese, a Liberian, a Libyan, a Liechtensteiner, a Lithuanian, a Luxembourger, a Macedonian, a Malagasy, a Malawian, a Malaysian, a Maldivan, a Malian, a Maltese, a Marshallese, a Mauritanian, a Mauritian, a Mexican, a Micronesian, a Moldovan, a Monacan, a Mongolian, a Moroccan, a Mosotho, a Motswana, a Mozambican, a Namibian, a Nauruan, a Nepalese, a New Zealander, a Nicaraguan, a Nigerian, a Nigerien,

a North Korean, a Northern Irishman, a Norwegian, an Omani, a Pakistani, a Palauan, a Palestinian, a Panamanian, a Papua New Guinean, a Paraguayan, a Peruvian, a Pole, a Portuguese, a Qatari, a Romanian, a Russian, a Rwandan, a Saint Lucian, a Salvadoran, a Samoan, a San Marinese, a Sao Tomean, a Saudi, a Scottish, a Senegalese, a Serbian, a Seychellois, a Sierra Leonean, a Singaporean, a Slovakian, a Slovenian, a Solomon Islander, a Somali, a South African, a South Korean, a Spaniard, a Sri Lankan, a Sudanese, a Surinamer, a Swazi, a Swede, a Swiss, a Syrian, a Tajik, a Tanzanian, a Togolese, a Tongan, a Trinidadian or Tobagonian, a Tunisian, a Turk, a Tuvaluan, a Ugandan, a Ukrainian, a Uruguayan, a Uzbekistani, a Venezuelan, a Vietnamese, a Welshman, a Yemenite, a Zambian and a Zimbabwean

all go to a bar..

The doorman stops them and says "Sorry, I can't let you in without a Thai."

Contents

Contents	iv
List of Figures	v
List of Tables	vii
1 The Dark Matter Story	3
2 Experiment Overview and Design	7
2.1 Sources of Power in Measured Spectrum	9
2.2 Toy Analysis	29
2.3 Thermal Noise in A Cavity	30
2.4 Reverberation Chambers and Statistical Uniformity	30
2.5 System Design	30
3 System Characterization and Data Acquisition	48
3.1 Control and Quantifying of Uncertainties	50
4 Data Analysis and Calibration	52
4.1 Hardware Injection Test	53
5 Beyond 300 MHz	68
Bibliography	69

List of Figures

1.1	Expected vs observed velocity distributions of M33	4
1.2	Dark matter mass regimes	6
2.1	Blackbody electric field spectral density from radio to UV frequencies	11
2.2	An antenna and matched resistor in cavities which are in thermal equilibrium.	14
2.3	Simulated antenna noise voltage at room temperature in the time domain	16
2.4	Simulated antenna noise power spectral density at room temperature in the frequency domain	17
2.5	Effect of averaging on simulated antenna noise power spectral density at room temperature in the frequency domain	18
2.6	Schematic of LNA adding input referred noise	23
2.7	Schematic of cascade of amplifiers and their added noise	25
2.8	Cascaded noise temperature for system with two amplifiers	26
2.9	Schematic of the RF receiver system	31
2.10	Spectrum from veto antenna during 300MHz data run	34
2.11	Photo of set up to measure Shielding effectiveness of shielded room	35
2.12	Shielding effectiveness of shielded room, 50-300 MHz	36
2.13	Shielding effectiveness of shielded room, 125-3000 MHz	37
2.14	AB-900A biconical antenna free space effective aperture, simulated, measured and theoretical	39
2.15	simulated AB-900A biconical antenna free space complex input impedance, vs measured biconical data	40
2.17	Schematic of Interlock board	42
2.18	Photo of lead-acid battery and slow turn on circuit	43
2.19	Acquisition efficiency for GPU-based Real-time spectrum analyzer	45
3.1	Data stream of real time DAQ. This set up is duplicated for channels A and B .	50
3.2	Gain vs. voltage of front end amplifier	50
4.1	Schematic of hardware injection test	55
4.2	Average S parameters of hardware injection test	56
4.3	Histogram of frequencies used for hardware injection test	59
4.4	Output-referred power spectral density from the hardware injection test	61

4.5	Standard deviation on output-referred power spectral density from the hardware injection test	62
4.6	Standard deviation of output-referred power spectral density from the hardware injection test, computed with median absolute deviation	63
4.7	Output-referred power spectrum from hardware injection test, various levels of zoom	65
4.8	Normalized, output-referred power spectrum from hardware injection test, various levels of zoom	66
4.9	Matched filtered, output-referred power spectrum from hardware injection test, various levels of zoom	67

List of Tables

2.1 Specifications for the spectrum analyzer used for run 1A.	44
---	----

Acknowledgments

Thank you to: Ben

Dave Hemmer

Monda

emiljia

Bill Tuck

Buchholtz/Ayars/Nelson/Kagan/Clare/Patrova/Rick Danner/pechkis

parents/janet/joel baba/papa

Belva

chatGPT

Mr keye

Bill Nye

Self plagiarism statement <https://journals.aps.org/copyrightFAQ.html>

As the author of an APS-published article, may I include my article or a portion of my article in my thesis or dissertation? Yes, the author has the right to use the article or a portion of the article in a thesis or dissertation without requesting permission from APS, provided the bibliographic citation and the APS copyright credit line are given on the appropriate pages.

<https://grad.ucdavis.edu/preparing-filing-your-thesis-or-dissertation>

Published or publishing pending material may be used with permission from the copyright owner, if not you, and the Graduate Chair, if you are not the first-author. See the Copyright FAQ for information about permissions when using published material.

Material you have authored, and which has been previously published or is pending publishing, may be used in its published format with three exceptions: 1) Margins - You must maintain 1" margins on all sides throughout the paper. 2) Pagination - page numbers must follow the UC Davis standards. 3) The title page must follow UC Davis standards and you must include an overall abstract.

comment: Need to add note about github and where code comes from

File: thesis.tex

Encoding: utf8

Sum count: 4743

Words in text: 3463

Words in headers: 78

Words outside text (captions, etc.): 1052

Number of headers: 19

Number of floats/tables/figures: 14

Number of math inlines: 142

Number of math displayed: 8

Subcounts:

text+headers+captions (#headers/#floats/#inlines/#displayed)

662+6+0 (2/0/0/0) _top_

369+4+71 (1/2/3/0) Chapter: The Dark Matter Story

310+4+0 (1/0/0/0) Chapter: Experiment Overview and Design

37+6+0 (1/0/0/1) Section: Sources of Power in Measured Spectrum

270+8+148 (3/1/47/6) Subsection: Thermal Noise

49+0+0 (0/0/24/0) Subsection: Dark Photon Signal

7+0+0 (0/0/4/0) Subsection: Radio Frequency Interference

30+0+0 (0/0/16/0) Subsection: Amplifier Chain Noise\codedir{thesis/ch2/CH2.ipynb}

6+0+0 (0/0/4/0) Subsection: ADC effects

9+0+0 (0/0/5/0) Subsection: Shielded room

2+0+0 (0/0/2/0) Subsection: Antenna

0+0+0 (0/0/0/0) Subsection: Spectrum Analyzer Details

309+5+16 (1/1/3/0) Chapter: System Characterization and Data Acquisition

0+5+0 (1/0/0/0) Section: Control and Quantifying of Uncertainties

5+6+7 (1/1/0/0) Subsection: Direct Measurement of Amp Chain Parameters

233+4+0 (1/0/1/0) Chapter: Data Analysis and Calibration

77+7+0 (1/0/0/0) Section: Hardware Injection Test \codedir{daqAnalysisAndExperiments/r

752+13+413 (3/3/30/1) Subsection: Injection test prerequisites

241+4+265 (1/3/1/0) Subsection: Performing the injection test

89+3+132 (1/3/2/0) Subsection: Inspection of Data

6+3+0 (1/0/0/0) Chapter: Beyond 300 MHz

(errors:2)

Chapter 1

The Dark Matter Story

If we start making a list of things that aren't here, we could be here all night. You know, pens for instance. Let's stick with things we can see.

Wheatley

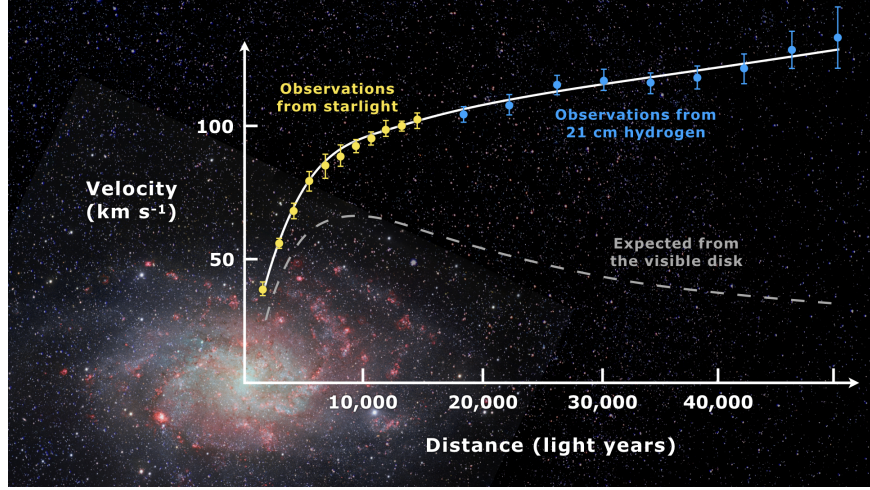


Figure 1.1: Expected vs observed velocity distributions of M33

It is believed that a large majority of the mass in the universe comes from an as yet undetermined source. This claim stems originally from work performed in 1933 by Fritz Zwicky who noticed a discrepancy between measured velocities of galaxies within the Coma Cluster and velocities predicted by applying the virial theorem. He wrote

If this [experimental result] would be confirmed we would get the surprising result that dark matter is present in much greater amount than luminous matter [1].

Vera Rubin furthered this work by measuring velocities of stars rotating in the M31 galaxy and concluded there must be additional non-luminous mass (originally published in [2], and shown in Fig.1.1). Studies of other phenomena, such as lensing (see [**lensing2**]) have confirmed the existence of this dark matter, and it is currently one of the major mysteries in modern physics.

Since the 1980's, the leading theories have consisted of an unknown species of elementary

particle. The search for weakly interacting massive particles (WIMPs) have dominated the budgets and schedules of the dark matter search effort but have yet to provide any experimental evidence.

In light of this, the 2017 community report on dark matter [3] highlights a need for a multi-experiment program in which many small scale experiments ($< \$10M$) split up to cover the vast landscape of potential dark matter candidates (see Fig. 1.2). Since very little is known about the dark matter, it is a playground for theoretical physicists to invent candidates. This overwhelming search should be narrowed down.

The enormous mass range splits nicely into two regimes; waves and particles. At a mass of order 1eV the inter-particle spacing \approx wavelength. Lighter than this it is more convenient to think of dark matter as a wave. Alternatively, dark matter candidates heavier than this are more conveniently modeled as exhibiting particle-like behavior. The Dark E-Field Radio experiment searches for dark photons in the nano- to milli-eV mass range where dark matter is best described as a wave. This property means one would search for a dark photon using wave-like detectors, e.g. antennas.

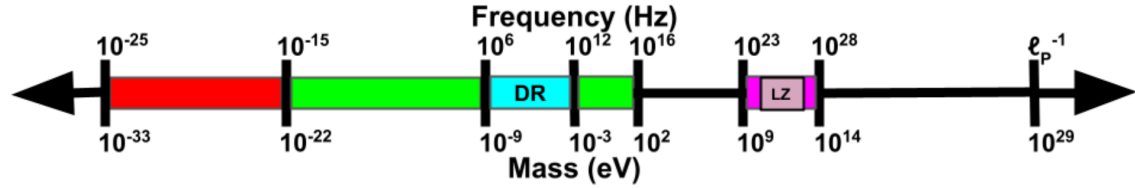


Figure 1.2: Cartoon depicting the mass scales over which dark matter may be found. Corresponding frequencies shown above. At heavy mass scales $> \mathcal{O}(1\text{ eV})$ the dark matter would behave like a particle, while on the lighter end it would behave like a wave. The Dark Radio Experiment searches at radio/microwave frequencies (blue) for a hidden photon using an antenna and spectrum analyzer. LUX-ZEPLIN Experiment (LZ) also shown.

Chapter 2

Experiment Overview and Design

A month in the laboratory can
often save an hour in the
library.

Frank Westheimer

Veljko Radeka said of detectors “One would imagine that in each particular case the best solution is arrived at by 1) the detector design to maximize the significant signal, 2) reduction of noise at its physical source, and 3) optimum filtering of signal and noise.” [4]. While he was referring to position sensitive particle detectors, the same three principles apply to this experiment. Put more directly, the goal is to maximize the signal to noise ratio. The detector in this case is a low-noise, wide-band radio receiver system searching not for discrete instances of particle-like interactions, but for coherent waves which are constant over long periods. The signal is a small excess of narrow-band, radio frequency power received by an antenna in a cavity. The noise is the white, thermal background due to the 300 K walls. The system is shown schematically in Fig. 2.9.

This chapter begins with a section titled Toy Analysis which walks through several back-of-the-envelope calculations to follow the signal and noise as it progresses from fields in free space through a simplified detector, resulting in a (simulated) dark photon detection. Through this section, several important concepts will come up and their implications can be analyzed. This will result in intuition which will explain the remaining design choices of Sec. 2.5. Furthermore, the actual experiment will report a null result, i.e. a lack of detection of a signal on a background. By following a signal *forward* through the system and data analysis, it will be more clear how to infer an exclusion limit from a power spectrum and working *backward* through the experiment.

In the following two sections, 2.3 and 2.4, effects will be introduced that were not apparent from the simplistic analysis of the first section. The final section, 2.5, details each piece of the system.

2.1 Sources of Power in Measured Spectrum

This section will break down each term in the following equation for the input-referred power

$$P_i = \text{Thermal Noise} + \text{Dark Photon Signal} + \text{RFI} + \text{Amp Chain Noise} + \text{ADC Effects}/G, \quad (2.1)$$

where G is a gain factor. While convenient, this word equation is not rigorous, and relies on the following subsections 2.1.1 - 2.1.5 for definition.

2.1.1 Thermal Noise

2.1.1.1 Blackbody Electric Field Density

This sub section estimates the noise-like¹ electric field in free space due to black body radiation. It assumes to be in *some* enclosure in that the ambient temperature is known to be 300 K and not the 3.6 K of the sky.

Planck's law gives the black body spectral energy density as

$$u_\nu(\nu, T) d\nu = \frac{8\pi h\nu^3}{c^3} \frac{1}{e^{h\nu/kT} - 1} d\nu \quad \left[\frac{J}{m^3} \right]. \quad (2.2)$$

This is frequently written in terms of spectral radiance,

$$B_\nu(\nu, T) d\nu = \frac{2h\nu^3}{c^2} \frac{1}{e^{h\nu/kT} - 1} d\nu d\Omega \quad \left[\frac{W}{m^2} \right]. \quad (2.3)$$

¹“Noise-like” simply means that the power contained in a signal is proportional to the bandwidth measured. Noise-like signals are more conveniently described as a power spectral density (PSD) which we will describe with the symbol S . As we will see, coherent signals which have finite width in frequency space $\Delta\nu_{\text{sig}}$ can share this property if the measurement bandwidth $\Delta\nu_{\text{RF}} \approx \Delta\nu_{\text{sig}}$, even though one wouldn't think of a coherent signal as being “noise-like”

Integrating this isotropic radiance over a solid angle 4π sr as well as a small frequency band $\Delta\nu$ gives the flux density $|\mathbf{S}|$ (AKA, the magnitude of the Poynting vector),

$$\begin{aligned} |\mathbf{S}| &= \int_0^{4\pi} \int_{\nu}^{\nu+\Delta\nu} B_{\nu}(\nu, T) d\nu d\Omega \\ &= \int_0^{4\pi} \int_{\nu}^{\nu+\Delta\nu} \frac{2h\nu^3}{c^2} \frac{1}{e^{h\nu/kT} - 1} d\nu d\Omega \quad \left[\frac{W}{m^2} \right]. \\ &\approx \frac{8\pi h\nu^3}{c^2} \frac{1}{e^{h\nu/kT} - 1} \Delta\nu \end{aligned} \quad (2.4)$$

The flux density can be related to the rms electric field from Poynting's theorem

$$|\mathbf{S}| = \frac{|E_{\text{rms}}|^2}{\eta} \quad \left[\frac{W}{m^2} \right], \quad (2.5)$$

where η is the impedance of free space. Equating Eqs. 2.4 and 2.5 and solving for the electric field gives

$$\frac{|E_{\text{rms}}|}{\sqrt{\Delta\nu}} = \sqrt{\eta \frac{8\pi h\nu^3}{c^2} \frac{1}{e^{h\nu/kT} - 1}} \quad \left[\frac{V}{m \cdot \sqrt{\text{Hz}}} \right], \quad (2.6)$$

and is plotted in Fig. 2.1.

Eq. 2.6 breaks up nicely into two regimes,

$$\frac{|E_{\text{rms}}|}{\sqrt{\Delta\nu}} = \begin{cases} \sqrt{\eta \frac{8\pi kT\nu^2}{c^2}} & \text{Rayleigh-Jeans regime } (h\nu \ll kT) \\ \sqrt{\eta \frac{8\pi h\nu^3}{c^2} e^{-h\nu/kT}} & \text{Wien approximation } (h\nu \gg kT) \end{cases} \quad \left[\frac{V}{m \cdot \sqrt{\text{Hz}}} \right]. \quad (2.7)$$

At frequencies and temperatures where the experiment is operated (< 300 MHz and 300K), $h\nu/kT \lesssim 5 \times 10^{-5}$ suggesting the Rayleigh-Jeans approximation is valid. At 300 K, this yields electric field spectral densities of 1 and $6 nV/m\sqrt{\text{Hz}}$ at 50 and 300MHz respectively.

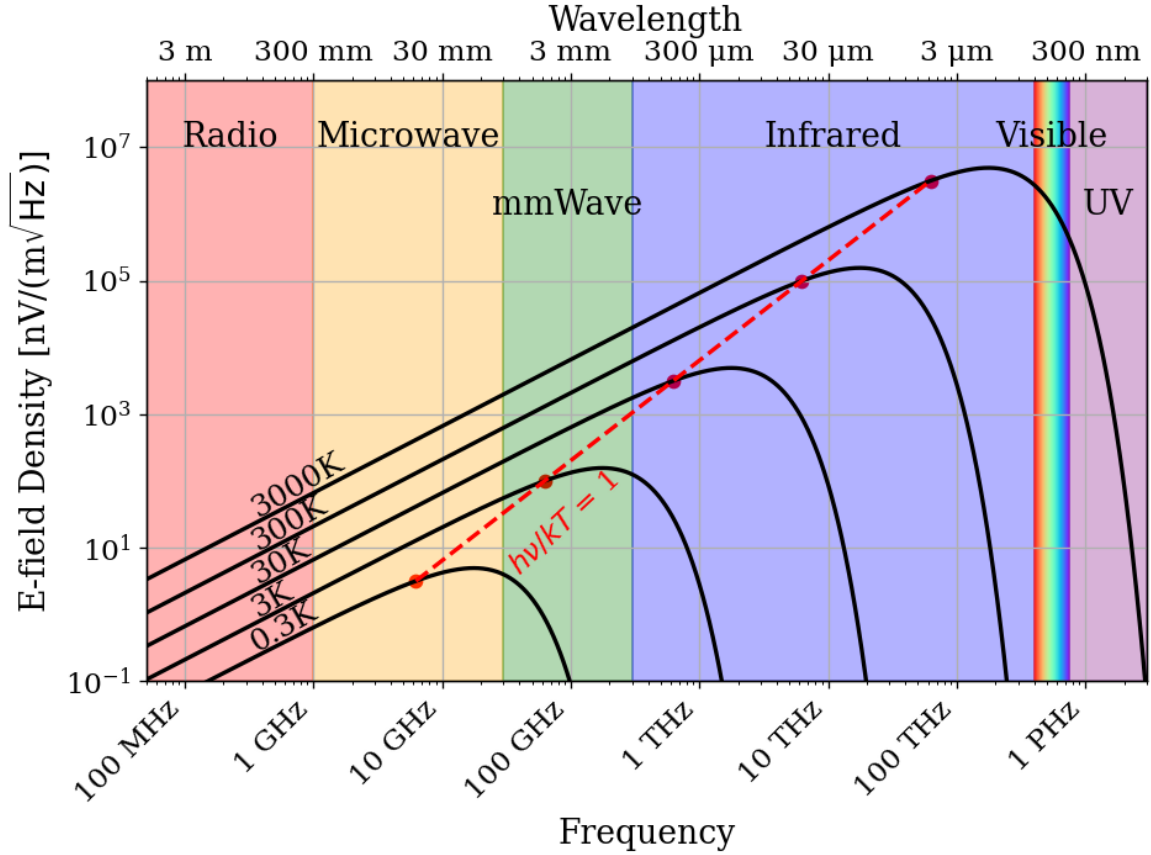


Figure 2.1: Blackbody electric field spectral density from radio to UV frequencies. A variety of temperatures are shown in black. The dashed red curve and red points indicate where along the black curves $h\nu = kT$, i.e. where Eq. 2.7 breaks up between the Rayleigh-Jeans regime to the Wien approximation. Note that these points are only a function of ν and T ; their vertical placement is chosen to lie on their respective curve but has no physical significance. The dark radio experiment is firmly in the Rayleigh-Jeans regime.

It is interesting to note, however, that for cryogenic experiments operating at a few GHz and in the sub K range, $h\nu/kT \approx 1$ and the full form of Eq. 2.6 must be used. This is shown at frequencies and temperatures to the right of the red dashed line in Fig. 2.1.

2.1.1.2 Antenna Noise

An antenna's effective aperture, A_e [m²], represents the effective area that it has to collect power density or irradiance [W/m²] from an incident Poynting vector,

$$P_A = |\mathbf{S}|A_e, \quad (2.8)$$

Where $|\mathbf{S}|$ is the magnitude of the incident Poynting vector and P_r is the power received at the antenna which is available at its terminals.

A_e is a directional quantity which varies with the antenna's directivity $D(\Omega)$, where Ω represents solid angle around the antenna. It varies with frequency ν , though it is generally discussed in terms of wavelength λ . Three matching parameters are introduced to describe how much actual power the antenna is able to deliver to a transmission line; p the polarization match of the wave to the antenna, m the impedance match of the antenna to the transmission line and η_a the efficiency of the antenna which represents how much power is absorbed compared to that lost to Joule heating of the antenna. p , m and η_a are all real, dimensionless and vary between 0 and 1.

$$A_e \equiv \frac{\lambda^2}{4\pi} D(\Omega) p m \eta_a. \quad (2.9)$$

This definition follows [5], though some authors do not include p in the definition [6] [7].

A simple derivation of the direction-averaged effective aperture based on thermodynamics will provide intuition. An isotropic antenna placed in a cavity at temperature T will be illuminated by randomly polarized, isotropic radiation of the form given by the Rayleigh-

Jeans limit of Eq. 2.4, $|\mathbf{S}| = 8\pi kT\Delta\nu\nu^2/c^2$. The power received by the antenna can be found by Eq. 2.8,

$$\begin{aligned} P_A &= \langle A_e \rangle \frac{1}{2} |\mathbf{S}| \\ &= \langle A_e \rangle \frac{4\pi kT\nu^2}{c^2} \Delta\nu, \end{aligned} \quad (2.10)$$

Where the factor of $1/2$ is introduced to account for the random polarization and the $\langle \cdot \rangle$ indicate an average aperture over all angles around the antenna. If a resistor is placed in a second cavity, also at temperature T , by it will deliver

$$P_R = kT\Delta\nu \quad (2.11)$$

into a matched transmission line. This is shown in Fig. 2.2. The second law of thermodynamics makes a very powerful statement here; the net power flow must equal 0 if the two temperatures are indeed equivalent. This means $P_R = P_A$ or Eq. 2.10 = Eq. 2.12,

$$\begin{aligned} \langle A_e \rangle \frac{4\pi kT\nu^2}{c^2} \Delta\nu &= kT\Delta\nu \\ \langle A_e \rangle &= \frac{c^2}{4\pi\nu^2} \quad [\text{m}^2] \\ &= \frac{\lambda^2}{4\pi} \end{aligned} \quad (2.12)$$

This allows us to conclude that the power spectral density S_{ant} received by an antenna surrounded by an isotropic temperature is simply $kT\Delta\nu$ in the Rayleigh-Jeans limit of room temperatures and standard electronic frequencies. This gives a power which is equivalent to the well known result for a resistor at 290 K,

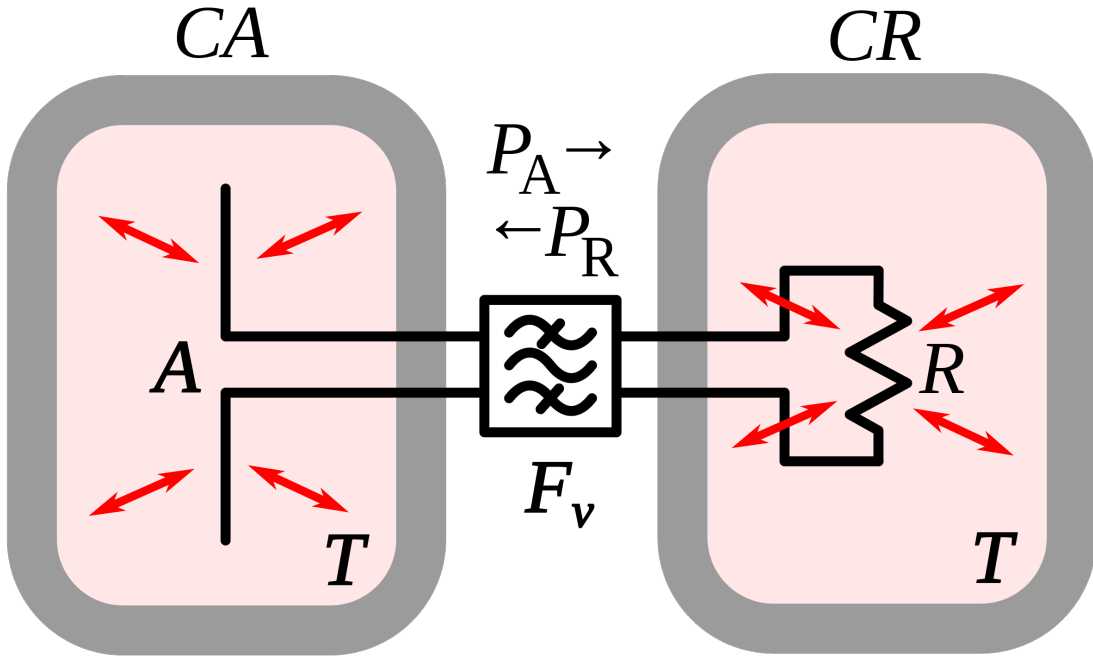


Figure 2.2: An antenna and matched resistor in cavities which are in thermal equilibrium. They are connected by a narrow filter permitting a narrow frequency band $\Delta\nu$. Image from Wikipedia.

$$S_{\text{ant}} = 3.9 \times 10^{-22} [\text{W}/\text{Hz}] = -174 [\text{dBm}/\text{Hz}]. \quad (2.13)$$

Note that S_{ant} indicates power spectral density and should not be confused with \mathbf{S} which indicates a Poynting vector.

2.1.1.3 Dicke radiometer equation

Equation 2.13 gave the mean of a power spectrum which is inherently noisy. We will now show the origin of this spectrum.

An enclosure who's electrically-lossy walls contain free charge carriers at finite temper-

ature will radiate incoherently by the fluctuation dissipation theorem. This theorem is the underlying principal of phenomena such as Brownian motion [8] and Johnson-Nyquest noise [9], but was not generally proven until 1951 by Callen and Wellton [10]. The random thermal fluctuation of the charge carriers will radiate a black body spectrum. Observing the electric field in the time domain, one can imagine the radiation arriving at a detector at a wide variety of random frequencies and phases. This is incoherent noise in that at each time domain sample is independent of the one proceeding it ². The detector will produce a voltage which can be modeled as a Gaussian with zero mean and standard deviation given by $\sqrt{S_{\text{ant}} \Delta\nu_{\text{RF}} |Z|}$ where Z is the system impedance (here 50Ω). This is shown for a room temperature antenna (or equivalently a room temperature resistor, see Fig. 2.2) in Fig. 2.3.

²The hidden assumption here is that blackbody radiation is totally incoherent. It actually has a coherence time $\tau_c \approx 2 \times 10^{-14} \text{ s}$ at 300 K [11]. For this statement to hold, the sample time $\tau_s \gg \tau_c$. For run 1A, $\tau_s = 1/800 \text{ MHz} = 1.25^{-9} \text{ s}$, 5 orders of magnitude more than τ_c

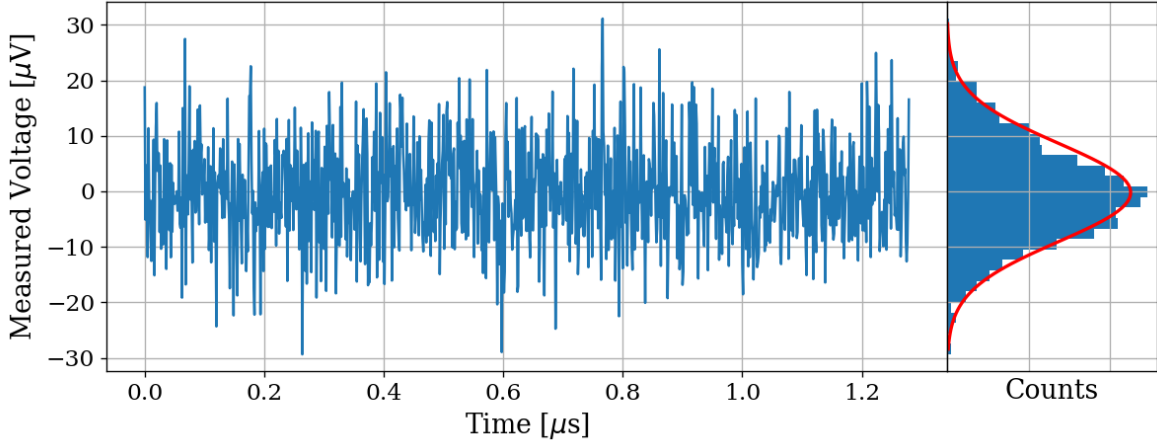


Figure 2.3: Simulated antenna noise voltage at room temperature in the time domain. Sample rate $\nu_s = 800\text{MHz}$ and number of samples $N = 2^{10} = 1024$. Bin width $\Delta\nu_{\text{RF}} = \nu_s/N \approx 800\text{ kHz}$. Data are binned and plotted as a histogram to the right. Best fit Gaussian is shown on the histogram in red with $\mu = -0.199\text{ }\mu\text{V}$ and $\sigma = 8.86\text{ }\mu\text{V}$. Counts have been normalized such that the bins add up to unity.

The next step in converting this time domain voltage signal to a frequency domain power spectral density (PSD). The first step is taking a discrete Fourier transform. This is usually implemented with an algorithm known as a fast Fourier transform (FFT), so that $\tilde{V} = \text{FFT}(V)$. In order to convert to a power spectrum, a non-trivial normalization prefactor must be included;

$$S = \frac{2}{N^2 |Z|} |\Re(\tilde{V})[:N//2]|^2, \quad (2.14)$$

where N is the number of samples, Z is the system impedance, and [:N//2] is python notation for the second half of the samples contained in the \tilde{V} array. Performing this operation on the data in Fig. 2.3 yealds the data in Fig. 2.4

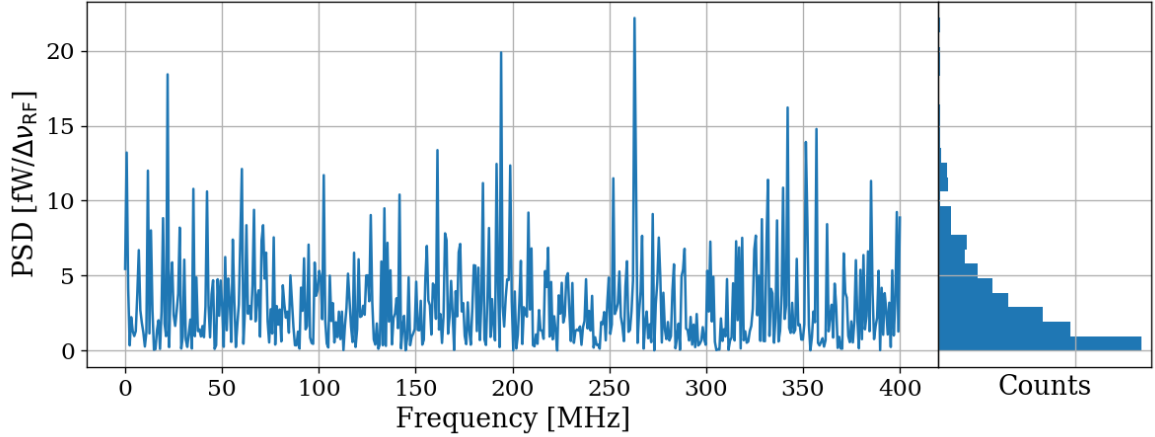


Figure 2.4: Simulated antenna noise power spectral density (PSD) at room temperature in the frequency domain. Sample rate $\nu_s = 800\text{MHz}$ and number of samples $N = 2^{10} = 1024$. Bin width $\Delta\nu_{\text{RF}} = \nu_s/N \approx 800\text{ kHz}$. Data are binned and plotted as a histogram to the right. Counts have been normalized such that the bins add up to unity.

The peculiar PDF of the histogram shown in Fig. 2.4 is known as a χ^2 distribution with 1 degree of freedom and comes about because power is a positive-definite quantity and the standard deviation of the PSD is greater than its mean.

However, by averaging many of these power spectra together the central limit theorem dictates that we can expect the resulting PDF to be Gaussian. The transition from χ^2 to Gaussian distributed spectra is shown in Fig. 2.5.

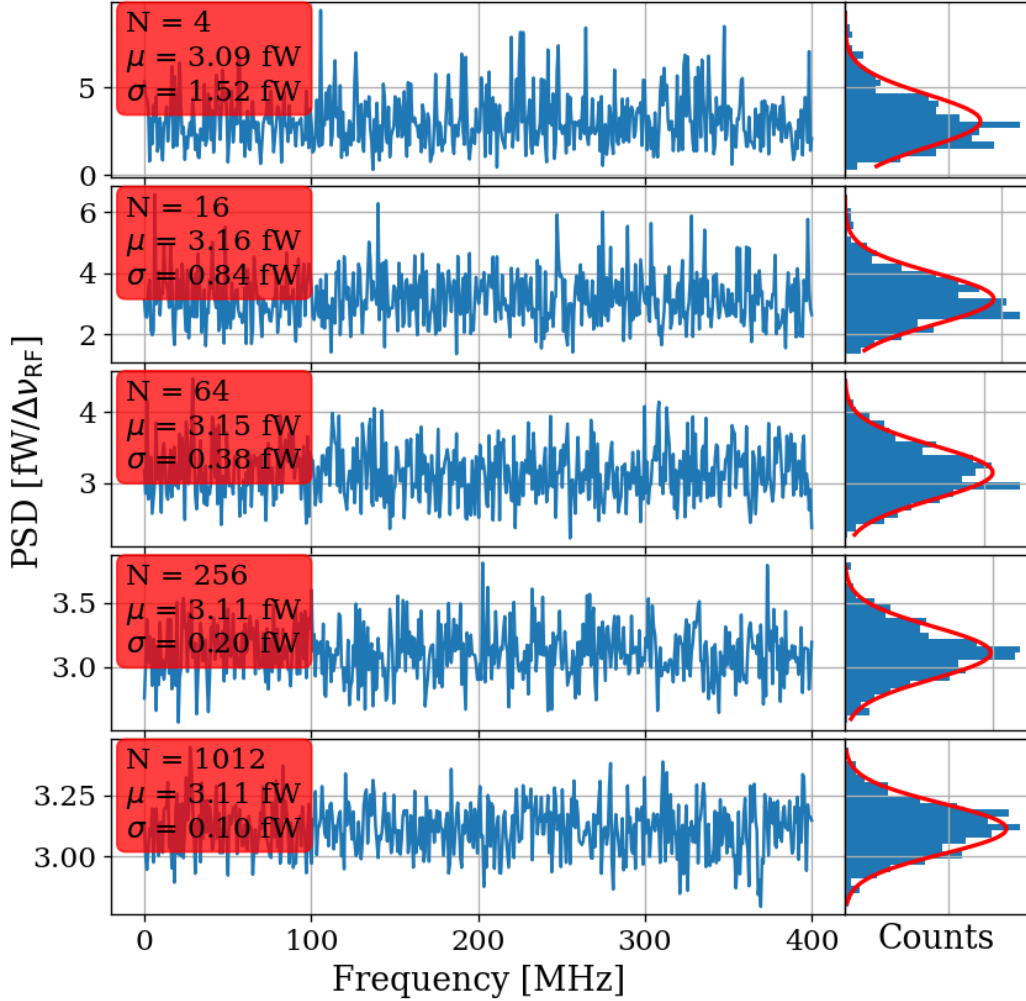


Figure 2.5: Effect of averaging on simulated antenna noise power spectral density (PSD) at room temperature in the frequency domain. Subplots show different number of averaged power spectra from $N = 4$ to 1024. Each subplot shows a factor of 4 times more averaging than the previous one. The Dicke radiometer equation predicts the standard deviation σ will scale like $N^{-1/2}$, once a large number of averages have been taken such that $\sigma \ll \mu$. Sample rate $\nu_s = 800\text{MHz}$ and number of samples $N = 2^{10} = 1024$. Bin width $\Delta\nu_{\text{RF}} = \nu_s/N \approx 800 \text{ kHz}$. Data are binned and plotted as a histogram to the right. Counts have been normalized such that the bins add up to unity.

Finally, this averaged power spectrum can be modeled with the Dicke radiometer equation. The measured power (assuming only thermal noise) is given by

$$P_{\text{ant}} = kT\Delta\nu \left(1 \pm \frac{1}{\sqrt{\Delta\nu\tau}}\right) \quad [\text{W}]. \quad (2.15)$$

Here τ is the total acquisition time and so $\Delta\nu\tau$ is equivalent to the number of spectra that are averaged together. This can be nondimensionalized and written

$$\frac{P_{\text{ant}}}{kT\Delta\nu_{\text{RF}}} = 1 \pm \frac{1}{\sqrt{N}} \quad [\text{W}], \quad (2.16)$$

which will become important during data analysis which is the topic of Ch. 4.

For the remainder of this thesis, unless otherwise stated, it will be assumed enough spectra have been averaged together that a PSD is Gaussian and scales with the square root of total acquisition time according to Eq. 2.15.

Thus far the analysis has focused only on thermal noise, however there are other sources of noise and interfering signals which must be considered, not to mention the actual dark photon signal.

2.1.2 Dark Photon Signal

The electric field of a kinetically mixed dark photon in free space $\mathbf{E}_{\text{ant}}^{\text{free space}}$ was derived in Sec. [add reference: XXX](#). In a cavity, the E-field will be enhanced by the quality factor Q of the cavity. This Q must be measured or simulated, but for this toy analysis we will assume

it to be known ³. The E-field inside the cavity then is

$$\mathbf{E}_{\text{ant}} = \mathbf{E}_{\text{ant}}^{\text{free space}} \sqrt{Q}, \quad (2.17)$$

since Q is proportional to power, i.e. \mathbf{E}^2 . This E-field will then need to be converted from a wave in the cavity to a wave in a 50Ω transmission line by an antenna. Similar to the thermal noise of the previous section, this electric field will be converted via the effective aperture of the antenna. Similar to Q , aperture will be assumed to be known.

The total received power from a coherent signal inside the room then is

$$P = \frac{\mathbf{E}_{\text{ant}}^{\text{free space}^2}}{\eta} Q < A_e >, \quad (2.18)$$

where η is the impedance of free space.

The observed spread of the frequencies of the dark photon are in important effect which determine system design. In the following paragraphs of this section, several sections of Gramolin et al. [13] are summarized, and the wording changed from “axion” to “dark photon” where appropriate, as well as a few variables slightly renamed to better match Levine et. al [add reference: levine et al.](#) Also note that the original calculation for the predicted line shape this appears to be Michael Turner in 1990 [14].

A simple model of the dark photon line assumes it is monochromatic, i.e. it's line shape is a delta function in frequency domain,

$$\nu_{\text{obs}} = \delta(\nu - \nu_{\text{DP}}). \quad (2.19)$$

This is consistent with it's production [add reference: misalignment mechanist/ch 1](#). However, when observed in a frame other than it's rest frame, the frequency of a (signal) dark

³Typical values are in the ball park of 100. Some experiments have ultra-high Q cavities $\approx 10^{10}$ [12]

photon will shift by an amount proportional to it's kinetic energy

$$\nu_{\text{obs}} = \left(1 + \frac{v_n^2}{2c^2}\right) \nu_{\text{DP}}, \quad (2.20)$$

where ν_{obs} is the observed frequency of the n th dark photon, v_n is it's velocity, c is the speed of light, and ν_{DP} is it's rest frequency. The end result will be a signal that has some spread in frequency, $\nu_{\text{DP}}/(\Delta\nu) \equiv Q_{\text{DP}} \approx 10^6$, with a line shape given by 2.23.

By summing over an infinity of dark photons of random phases and velocities (sampled from the relative velocity of the dark matter halo), each with a frequency given by Eq. 2.20, one can construct a power spectral density (PSD) of the dark photon signal as measured on earth, S [W/Hz].

When performing a measurement, one records the voltage V emerging from a detector for a period of time greater than the coherence of the dark photon $\tau_{\text{FFT}} \gg \tau_c$. The Fourier transform of $V(t)$ is denoted $\tilde{V}(\nu)$

The signal will have a total power

$$P_0 = \frac{1}{\tau_{\text{FFT}}} \int_0^{\tau_{\text{FFT}}} \frac{|V(t)|^2}{|Z|} dt = \int_0^{1/\tau_{\text{FFT}}} S(\nu)^2 d\nu, \quad (2.21)$$

which is a statement of Parseval's theorem.

The normalized line shape is defined by dividing by P_0 ; $\lambda(\nu) \equiv S(\nu)/P_0$. This has the property of being normalized to unity,

$$\int_0^\infty \lambda(\nu) d\nu = 1. \quad (2.22)$$

Finally, the result for this normalized line shape is

$$\lambda(\nu) = \frac{2 c^2}{\sqrt{\pi} v_0 v_{\text{lab}} \nu_{\text{DP}}} \exp \left(-\frac{\beta^2 v_0^2}{4 v_{\text{lab}}^2} - \frac{v_{\text{lab}}^2}{v_0^2} \right) \sinh \beta \quad \left[\frac{1}{\text{Hz}} \right], \quad (2.23)$$

where $|v_0| \approx 220$ km/s is the circular rotation speed of the Galaxy at the radius of the sun (approximately 8 kpc), $v_{\text{lab}} \approx 233$ km/s is the relative velocity of the Sun to the rest frame of the Galaxy and

$$\beta \equiv \frac{2 c v_{\text{lab}}}{v_0^2} \sqrt{\frac{2(\nu - \nu_{\text{DP}})}{\nu_{\text{DP}}}}.$$

Equation 2.23 is plotted in Fig. [add reference: line shape in toy analysis](#). Note it's quality factor $Q_{\text{DP}} \approx 10^6$ as mentioned above.

2.1.3 Radio Frequency Interference

Radio Frequency Interference (RFI) includes any coherent interfering signals which can be detected by the experiment. While noise is better described as a power spectral density [W/Hz] or electric field density [V/(m $\sqrt{\text{Hz}}$)], RFI is made up of more narrow lines and is discussed in terms of a power [W] or electric field [V/m]. In this experiment, RFI is mitigated through the shielding effectiveness (SE) of the cavity. SE measurements and more details about local RFI are discussed further in Sec. 2.5.1, and a plot of the local RFI spectrum is shown in Fig. 2.10.

The peak RFI spike is at 186 MHz and approximately 100 $\mu\text{V}/\text{m}$, an energy density of roughly 10^{-11} W/m². This will be reduced by the SE of the room (roughly 120 dB at 200MHz, see Fig. 2.11), but just like a coherent dark photon, it will be enhanced by the

$Q/\text{effective aperture}$. This will be right on the edge of detection, but in the actual date run it was not detected.

2.1.4 Amplifier Chain Noise⁴

Any amplifier will have some noise which it adds to an incoming signal which will degrade the signal to noise ratio (SNR) of the measurement⁵. A low noise amplifier (LNA) is an amplifier which has been specifically designed to minimize the noise contribution. This process is shown schematically in Fig. 2.6.

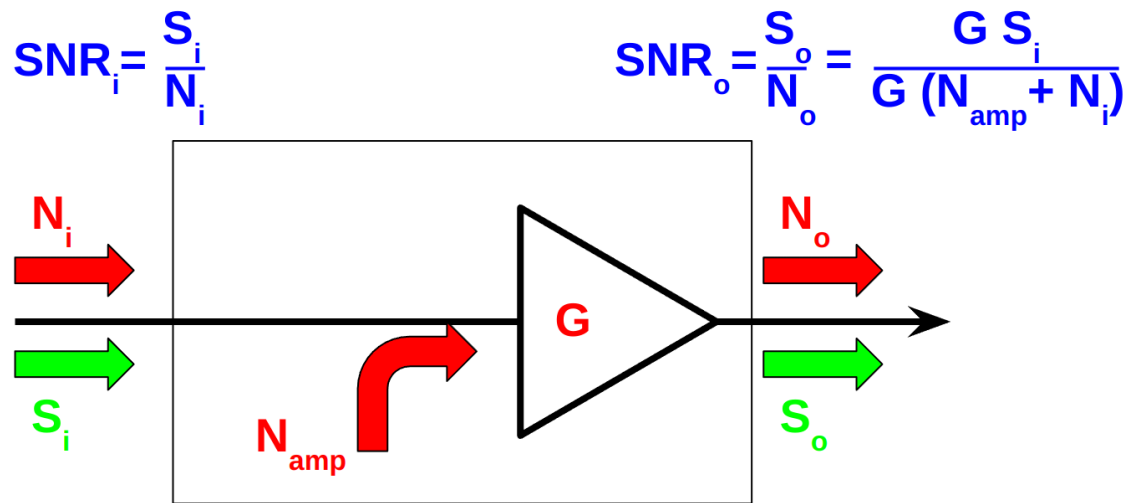


Figure 2.6: Schematic of LNA adding input referred noise N_{amp} . Since N_{amp} is referred to the input, it can be directly added to the input noise which is itself input-referred. The amplifier (depicted as a triangle) is assumed to be noiseless, while the physical amplifier including noise is contained in the rectangle.

⁴Code for this section can be found at: <https://github.com/josephmlev/darkRadio/tree/master/thesis/ch2/CH2.ipynb>

⁵A great lecture on the subject by Prof. Greg Durgin can be found at [15]

The performance of an LNA is generally evaluated by a figures of merit and noise factor (F). F is defined to be the ratio the SNR at the input of an LNA to that at its output.

$$\begin{aligned}
F &\equiv \frac{\text{SNR}_i}{\text{SNR}_o} \\
&= \frac{S/N}{[S G]/[(N + N_{\text{amp}})G]} \\
&= \frac{1}{1/[1 + N_{\text{amp}}/N]} \\
&= 1 + \frac{N_{\text{amp}}}{N},
\end{aligned} \tag{2.24}$$

where S and N are the signal and noise [W] presented to the LNA respectively, N_{amp} is the input-referred noise added by the LNA and G is the gain. By factoring out the implicit $k \Delta\nu$ from $N = kT\Delta\nu$, we find

$$F = 1 + \frac{T_e}{T_0}, \tag{2.25}$$

where T_e is the noise temperature of a device and T_0 the temperature of the system being measured by the LNA.

Note that following the same derivation as Eq. 2.24, it is simple to show that the noise figure of an attenuator at temperature T with loss L is given by

$$F_{\text{att}} = 1 + \frac{(L - 1)T}{T_0}, \tag{2.26}$$

where T_0 is the reference temperature defined above. If $T = T_0$, Eq. 2.26 simplifies to $F_{\text{att}} = L$

In order to standardize device specifications for across system applications, it is common to choose a reference temperature T_0 of 290K. If not specified, it is generally safe to assume this has been done.

Noise factor is simply defined from noise figure,

$$\text{NF} \equiv 10\log_{10}(F). \quad (2.27)$$

When working with LNAs, all three measurements (T_e , F and NF) are frequently used and one must use Eqs. 2.25 and 2.27 to convert between them.

One important generalization is that of a cascaded series of amplifiers, shown schematically in Fig. 2.7.

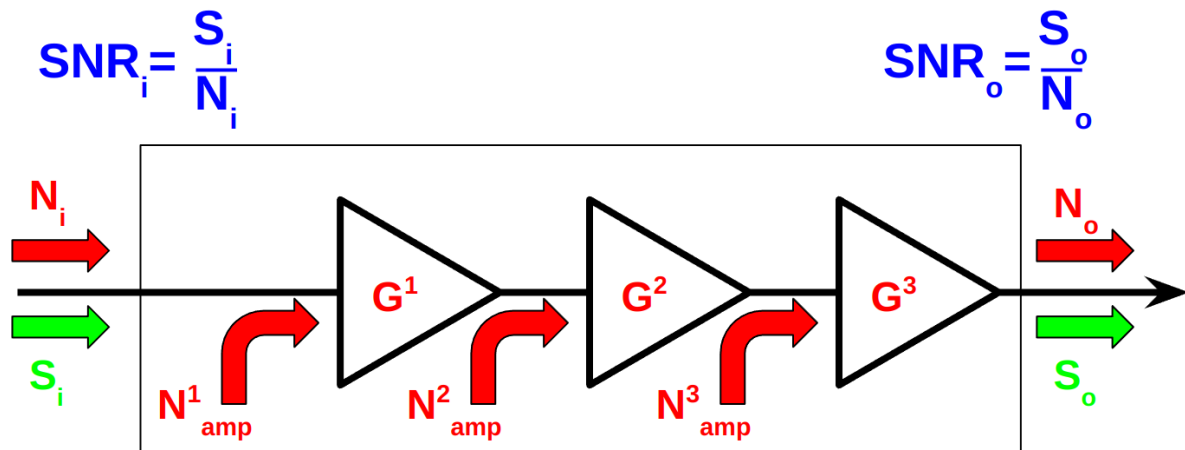


Figure 2.7: Schematic of cascade of $n = 3$ amplifiers and their added noise N_{amp}^n . Each amplifier has a gain of G^n . The SNR at the output is derived in Eq. 2.28. Note that superscripts in the figure and caption refer to index of each component and are not exponents.

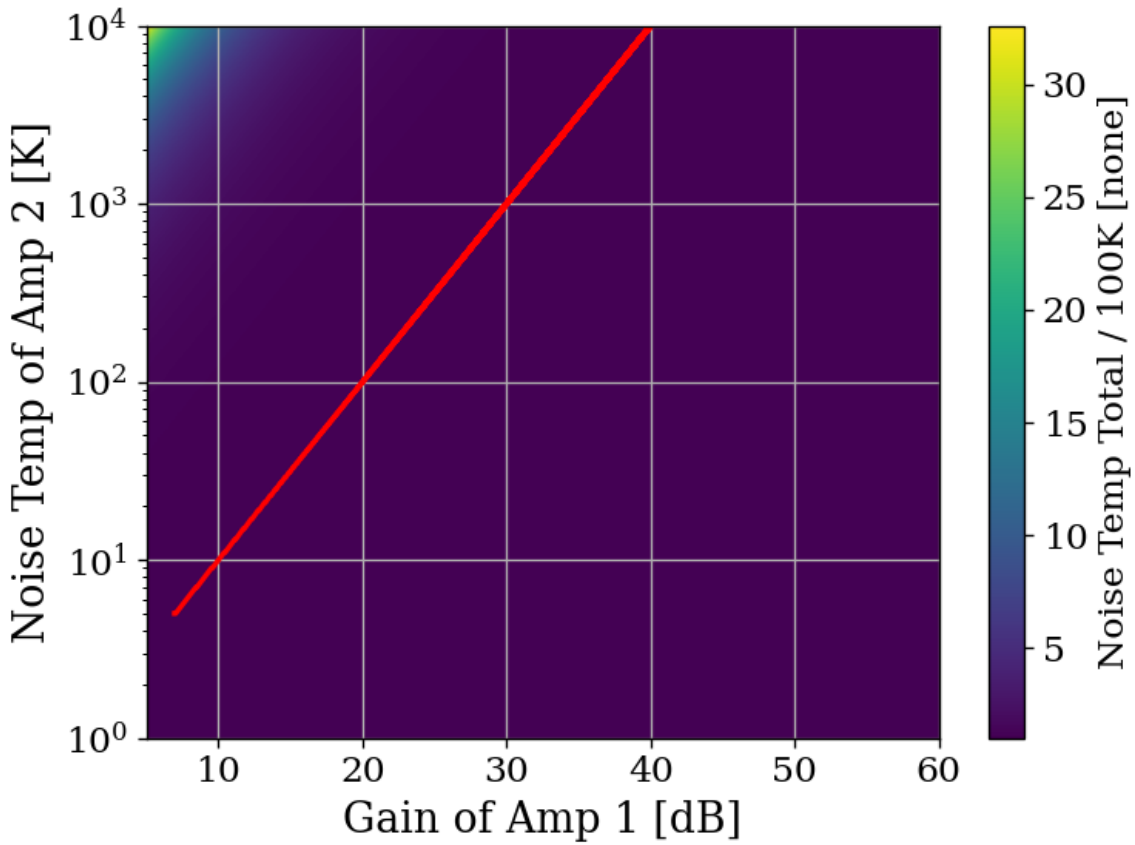


Figure 2.8: Cascaded noise temperature for system with $n = 2$ amplifiers, normalized to noise temperature of amplifier 1 (the so called LNA) = 100 K. Shown schematically (for $n = 3$) in Fig. 2.7. First amplifier's noise temperature and gain (40 dB and 100 K respectively) roughly equivalent to the LNA used in phase 1A of the experiment[16]. Red curve shows where the system's noise temperature is 1% higher than LNA noise temperature. This shows that for a 40 dB, 100 K LNA, in order to change the system noise temperature by 1 K, a second stage amplifier with a noise temperature of 10^4 would be required. Secondary amplifiers with noise temperatures closer to 500 K are realistic and inexpensive. Note that red curve should continue, but is cut off as a plotting artifact.

Here the total noise figure of n amplifiers can be shown to be

$$F_{\text{total}} = F_1 + \frac{F_2 - 1}{G_1} + \frac{F_3 - 1}{G_1 G_2} + \cdots + \frac{F_n - 1}{G_1 G_2 \cdots G_{n-1}}, \quad (2.28)$$

following the same derivation as Eq. 2.24. Since the noise temperature of a system depends

on the noise temperature a given amplifier divided by he gain which precedes it, a front-end LNA with modest gain ensures the total noise figure of the the system is equal to it's noise figure to very good approximation. This is shown in Fig. 2.8. We will use this approximation and assert

$$\text{Amp Chain Noise} = \text{LNA Noise}, \quad (2.29)$$

Where LNA here is taken to mean the first gain stage in the amplifier chain
 Noise figures are typically frequency dependant, though they vary slowly over frequency and can be approximated as constant over narrow frequency bands. Noise figures are typically given on the data sheet of the LNA [16], but can also be measured. Measurement of LNA noise is covered in Sec. [add reference: ch 3](#) and is shown in Fig. [add reference: LNA NF](#) (which is in good agreement with the LNA's data sheet [16]).

The power contributed by the LNA's noise is simply given by

$$P_{\text{LNA}} = kT_e\Delta\nu \quad (2.30)$$

This is again the mean of a fluctuating power, just as 2.15.

2.1.5 ADC effects

“ADC effects” is a catch all term which refers to power introduced by an analog-to-digital converter. It contains are a three components, listed in order of importance;

$$\text{ADC Effects} = \text{Spurious Signals} + \text{ADC Noise Floor} \quad (2.31)$$

Equation 2.28 shows that gain G introduced before a noisy element in the RF chain, will reduce the relative contribution of that noise by a factor of G . The same idea applies to ADC effects, though one must be careful with the language used to describe this; spurious *signals* are not noise, and the experiment's output *is* mostly noise.

2.1.5.1 Spurious signals

Spurious signals (also known as spurs) are coherent signals which are introduced into the signal at the ADC⁶. They are likely caused by RFI due to various clocks in the PC in close proximity to the ADC. The coherence of spurs means they will pop up above the noise with more averaging. Spurs don't degrade the SNR of the experiment in the same way a noisy amplifier chain would; they produce false positive candidates which must be excluded, similar to RFI discussed in Sec. 2.1.3. Similar to ADC noise, they can be measured easily by terminating the input of the ADC and scanning. They are investigated thoroughly in Sec. [add reference: spur testing, ch 3](#), where they are shown to be nearly negligible, having been mitigated by the gain of the system. There is a single spur detected after a few days (see sec [add reference: fasle positive](#)), but for this simple analysis we will assume spurs are negligible.

⁶Note that these spurs described here are not the same as the spurs that are described by the ADC specification *spur free dynamic range* (SFDR). SFDR is measured in dBc, i.e. *relative* to a carrier. Since our “carrier” is broadband noise, each bin produces some spurs which are -66 dBc [17] relative to itself. These spurs are also broadband, and average down with the experiment’s noise. The SFDR spurs are negligible

2.1.5.2 ADC noise

ADC noise can simply be measured by terminating the input and taking a scan. This is shown in Fig. [add reference: terminated input](#). The result is that ADC noise is a factor of 10^5 lower than the thermal noise of the experiment, both output-referred⁷, which agrees with the ADC's data sheet [17]. Since ADC noise follows the same scaling as the experiment's thermal noise (Eq. 2.15), this factor of 10^5 is independent of averaging, and ADC noise is totally negligible.

2.2 Toy Analysis⁸

With each of the terms of Eq. 2.1 defined in the previous section, we will now perform view several simulations which will provide intuition about the process of detecting a weak, narrow signal on a background PSD of thermal noise which has been averaged a sufficient number of times such that it's PDF is Gaussian.

⁷Technically it doesn't matter where they are referred since they are taken in ratio. As long as they are referred to the same point!

⁸Code for this section can be found at: <https://github.com/josephmlev/darkRadio/tree/master/thesis/ch2/toyAnalysis.ipynb>

2.3 Thermal Noise in A Cavity

2.4 Reverberation Chambers and Statistical Uniformity

Generally it is convenient to think of electromagnetic cavities as containing a single mode

2.5 System Design

This section outlines the subsystems which make up the experiment. While specifics and basic calculations are provided as they apply to design choices of subsystems, testing and characterisation of the system as a whole is covered in Ch. 3 and calibration of the system is discussed in Ch. 4.

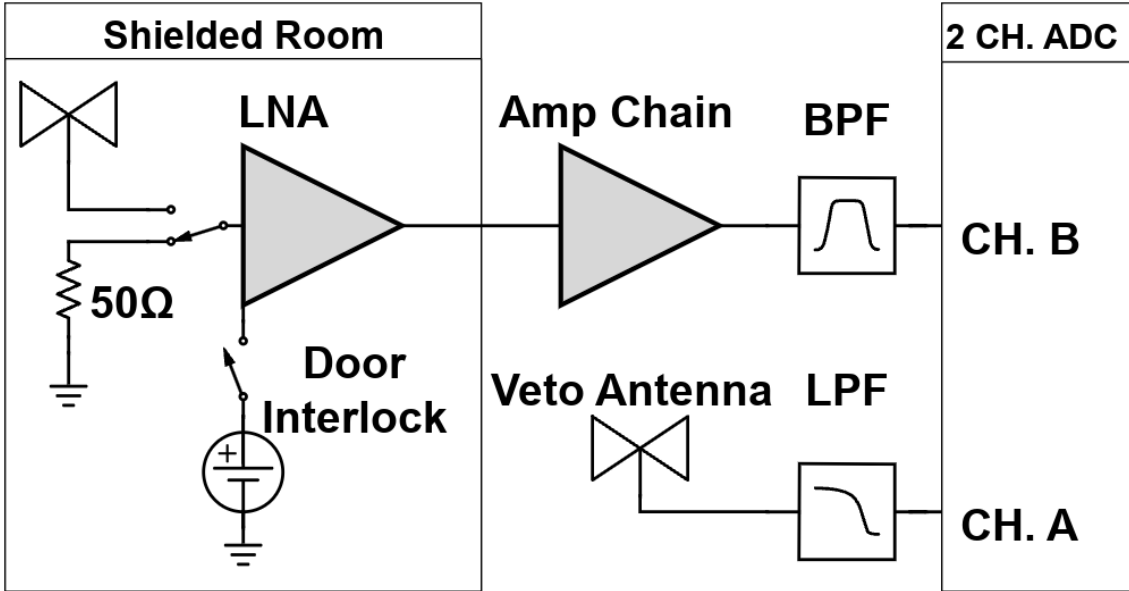


Figure 2.9: Schematic of the RF receiver system. An RF coax switch allows the PC to control the source (antenna or terminator). The switch is controlled by optical fiber to maintain isolation of the room. The LNA (Pasternack PE15A1012) has a nominal gain and noise temperature of 40dB and 100K (Figs. XXX and XXX). It is interlocked (Fig. 2.17) to the door to protect amp B and the ADC from large signals when the door is open. The secondary amplifier is a miniCircuits (MC) ZKL-1R5+ and has a nominal gain of 38dB. Not pictured after this amplifier is a fixed 4dB of attenuation. The band pass filter (BPF) is made up of a MC SLP-50+ high pass filter (HPF) and a MC ZX75LP-288-S+ low pass filter. The HPF reduces the bandwidth and therefore the total power of the signal before entering the ADC allowing for more gain before clipping. The LPF serves the same purpose while also acting as an anti-aliasing filter. These two filters define the experiment's bandwidth, $-3 \text{ dB} \approx 40 - 320 \text{ MHz}$. The veto antenna is outside of the room and interference is not reduced by the $\approx 100 \text{ dB}$ SE of the room, so no gain is required. The LPF on the veto is for anti-aliasing.

2.5.1 Shielded room

The shielding room [18] serves two purposes. The first is straightforward; to shield the antenna, keeping radio frequency interference (RFI) *out*. The second purpose is a bit more subtle; to keep any converted dark photons *in*. This second point is addressed further as an

aspect of system calibration in Ch. 4, but roughly can be described by the loaded quality factor [19–21] of the antenna/room system. Namely, a more resonant system will be more sensitive to coherent signals. This subsection will focus on the first point, keeping RFI out.

Shielding effectiveness SE is a measurement of a shielding enclosure’s ability to attenuate electromagnetic waves from entering,

$$SE \equiv 10 \log_{10} \left(\frac{P_{\text{open}}}{P_{\text{closed}}} \right) = P_{\text{open}, dB} - P_{\text{closed}, dB} \quad (2.32)$$

where $P_{\text{open}}/P_{\text{closed}}$ are powers received with the door open/closed. The ratio of powers allows all the specifics of antenna matching to cancel allowing for a very simple measurement.

Due to reciprocity between antennas, this is equivalent to measuring the attenuation of waves leaving. The latter method is simpler and was performed. The IEEE standard prescribing a very detailed SE measurement procedure [22] was used as a rough guideline but the simple results presented here should be viewed as an estimate.

The SE was measured by placing a Rigol DSG-830 signal generator inside the room, powered by the filtered 12 VAC Edison outlets inside the room. An antenna (bicon or Vivaldi) was connected to the signal generator. Outside of the room, an identical antenna (again, bicon or Vivaldi) was connected to a Rigol RSA-5065-TG spectrum analyzer. The spectrum is scanned to find a frequency without local interference which would confuse the results. The spectrum analyzer was set to attenuate its input to prevent clipping⁹, and the signal generator was set to output a sine wave at maximum power. The power measured on

⁹The spectrum analyzer automatically calibrates the displayed spectrum to its internal attenuator and pre-amplifier. If external gain/attenuation are used, they must be accounted for manually.

the spectrum analyzer is P_{open} of Eq. 2.32. The door was closed, attenuation removed and P_{closed} was measured. In some cases the SE was so high a signal was buried below the noise floor of the spectrum analyzer. These data are shown in red in Figs. 2.12 2.13.

SE can drop off to less than 80dB if the RF gasket around the door is not clean. Previous day-long test runs detected several hundred signals which originated from RFI emitted from the PC and several local radio stations. Cleaning was performed by scrubbing the copper gasket and steel mating surface with red scotch-brite using denatured alcohol as a lubricant. After two passes of polishing were complete, a layer of Deoxit D100L liquid was added. Maintenance cleanings were performed using only Deoxit D5 spray. These signals were not detected after the gasket was cleaned, which is consistent with calculations of Sec. XXX

The primary RFI in the 50-300 MHz span are from local radio broadcasts. The strongest of this is around $100 \mu\text{V}/\text{m}$ as measured in the lab. There are also many lower level peaks which span the entire frequency range, though are more pronounced in a few frequency bands (60-75MHz, 130-140Mhz, 270-290MHz). These peaks come from the PC which serves as the spectrum analyzer. Before the door was cleaned, many of these signals were detectable, but cleaning the door resulted in a clean spectrum for the 9 day data run. The spectrum from the veto antenna (discussed in Sec. XXX) is shown in Fig. 2.10

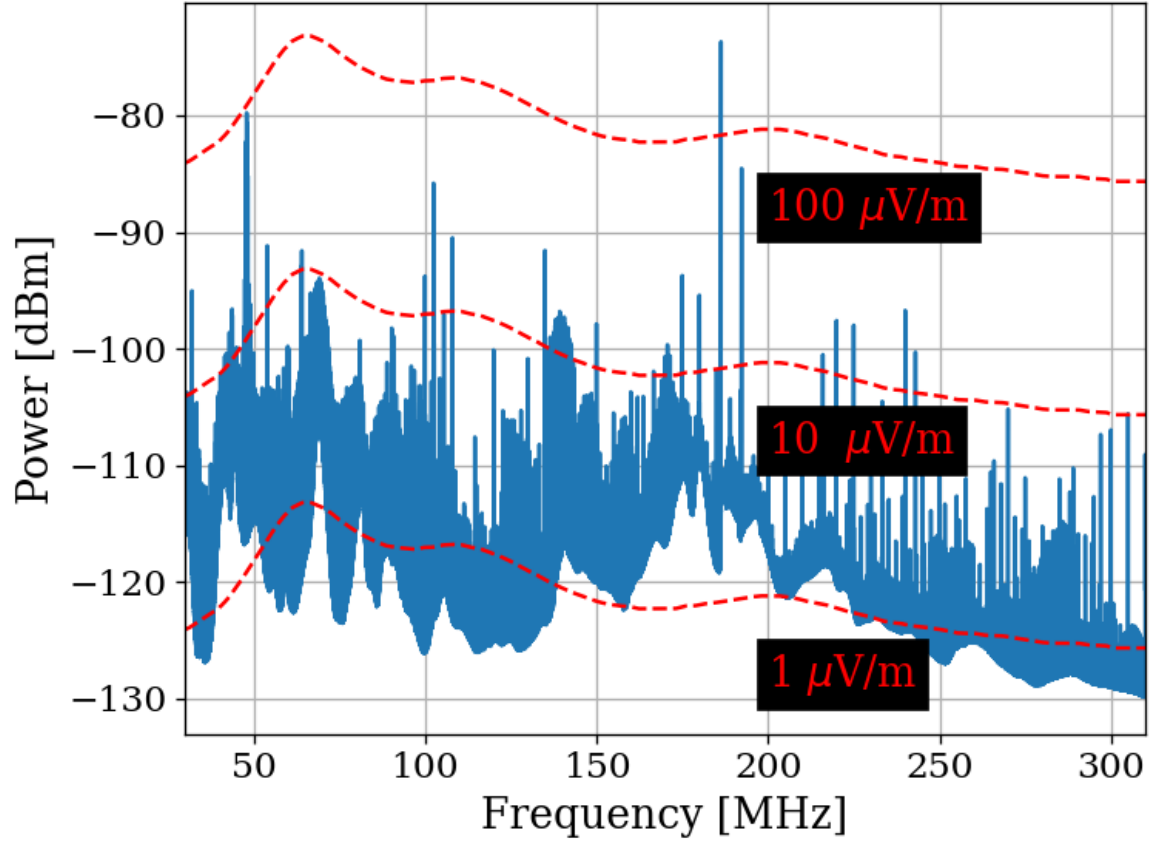


Figure 2.10: Spectrum from veto antenna during 300MHz data run. Spectrum plotted as measured power in dBm. Red curves indicate the equivalent field strength. The curves track the antenna factor with frequency for the COMPOWER AB900 [23] bicon. Two identical AB900 antennas are used, one to search for dark photons in the shielded room, and a second to monitor the local RFI background.



Figure 2.11: Photo showing set up to measure SE of 314. Photo taken using Vivaldi antennas for data shown in Fig. 2.13. The same set up was used with bicon antennas for the 50-300 MHz data shown in Fig. 2.12. Bicon antenna shown in background of photo was not in use for this test.

314 Shielding Effectiveness

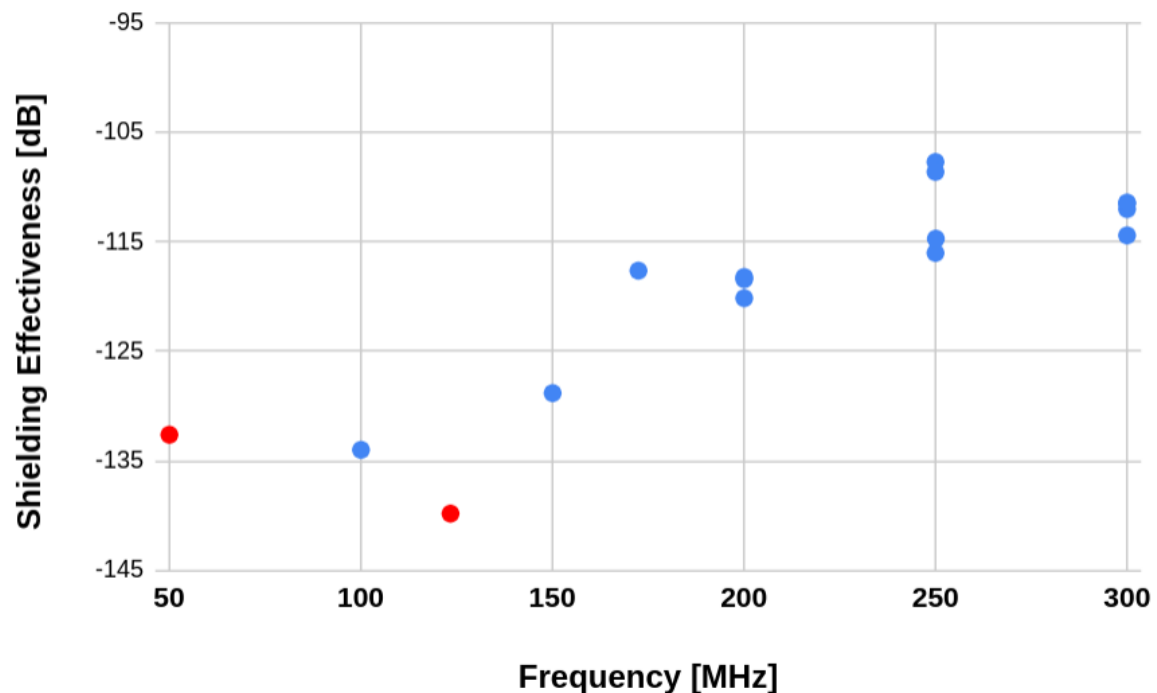


Figure 2.12: Shielding effectiveness of shielded room measured with Bicon antenna. Red points indicate measurements limited by the noise floor of the spectrum analyzer located outside and are an upper limit; true SE is lower (better). Measurement would require a stronger amplifier inside the room. At a few frequencies the antenna inside the room was moved to get a sense of the uncertainty of the measurement.

314 Shielding Effectiveness

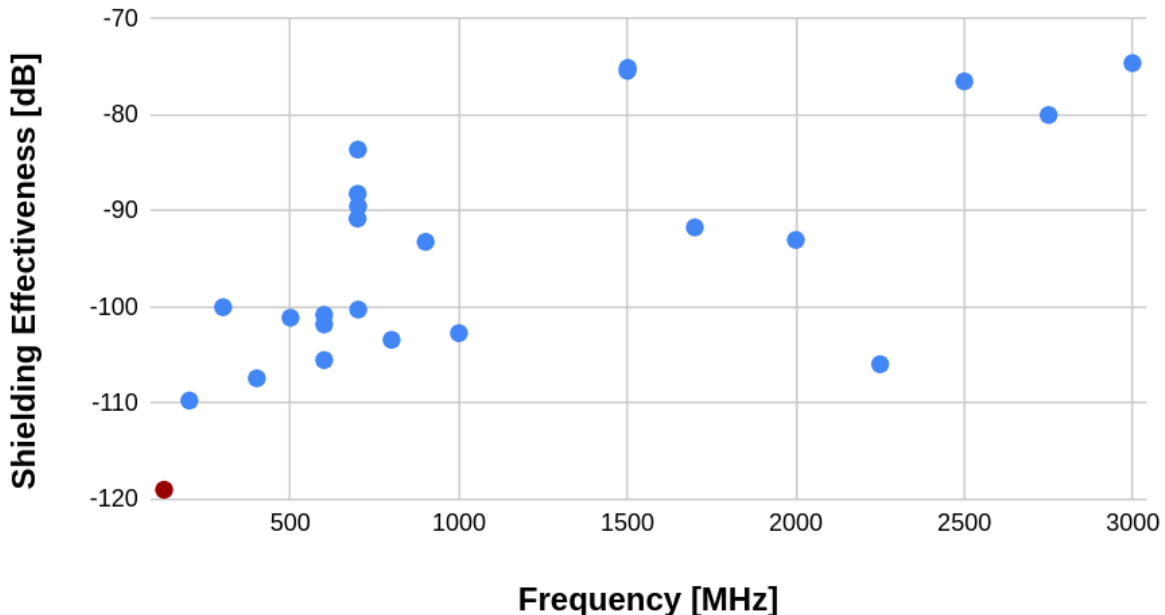


Figure 2.13: Shielding effectiveness of shielded room measured with Vivaldi antenna. Red points indicate measurements limited by the noise floor of the spectrum analyzer located outside and are an upper limit; true SE is lower (better). Measurement would require a stronger amplifier inside the room. At a few frequencies the antenna inside the room was moved to get a sense of the uncertainty of the measurement.

2.5.2 Antenna

The antenna plays an important roll in the experiment as the matching device between electromagnetic waves in the cavity and the receiver system. For a broadband search such as the 50-300 MHz run (a 6:1 bandwidth), a broadband antenna must be used. The chosen antenna must provide a good impedance match and high efficiency since an inefficient antenna would convert a substantial amount of the converted dark photon's power into heat in the antenna's structure. For the 50-300 MHz run, a ≈ 131 cm biconical antenna (bicon) was chosen. The selected model is manufactured by COMPOWER, model AB-900A [23]. In a phone call with the manufacturer as well as testing of the isolated balon, it was determined that the balun used in the antenna was 1:1. This allows for simple simulation. In COMSOL, the lumped port option allows for a balanced drive of an antenna. A match to a 50Ω transmission line through a 1:1 balun is simply modeled as a lumped port, a very simple object in COMSOL featured in nearly all of the antenna tutorials¹⁰

¹⁰See for example the dipole antenna tutorial, available at <https://www.comsol.com/model/dipole-antenna-8715>

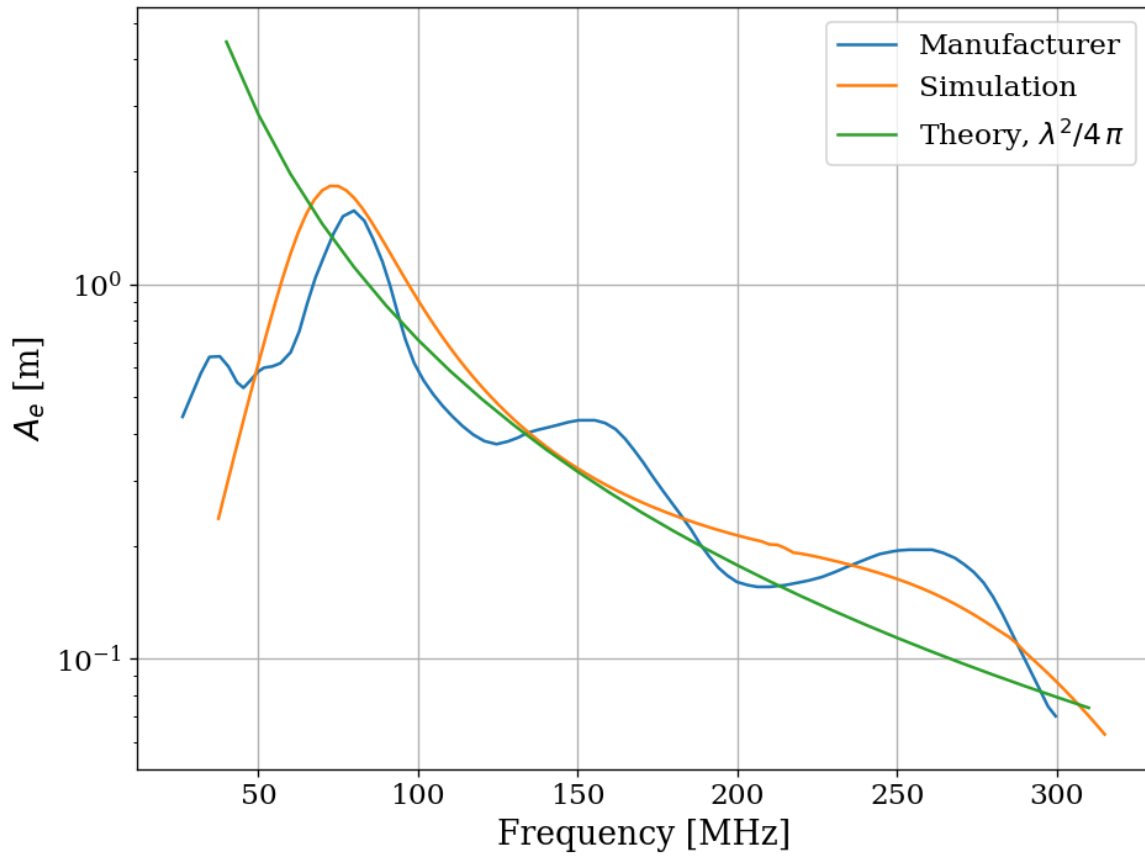


Figure 2.14: AB-900A biconical antenna effective aperture, simulated, measured and theoretical in free space. Simulation performed in COMSOL. The measurement was provided by manufacture [23] as an antenna factor and was converted using Eq. xxxx.

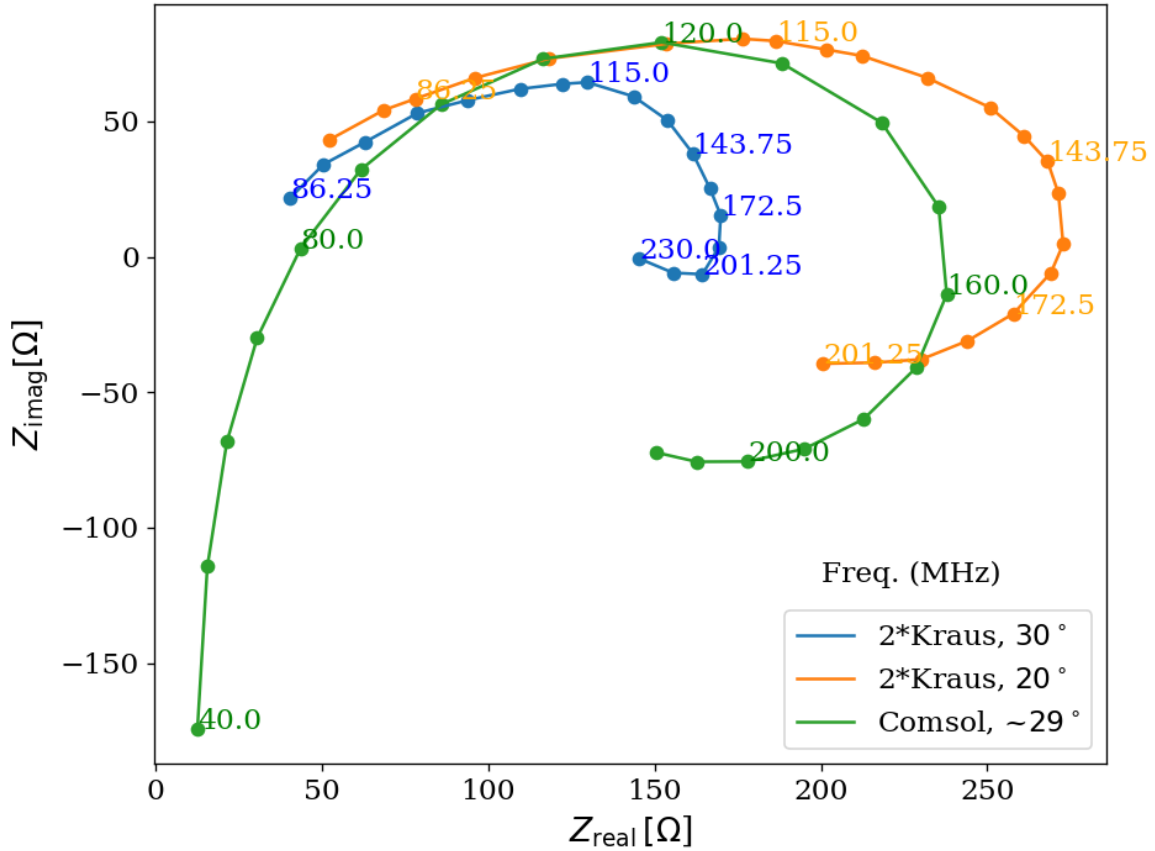


Figure 2.15: Simulated AB-900A biconical antenna free space complex input impedance shown in blue. Simulation was performed in COMSOL. Measurement from Kraus, second edition, Fig 8-13 [24], reproduced here in Fig. 2.16. Measured data is for a monoconical antenna and must be multiplied by 2 to compare to a biconical antenna. Numbers along curve indicate frequency in MHz.

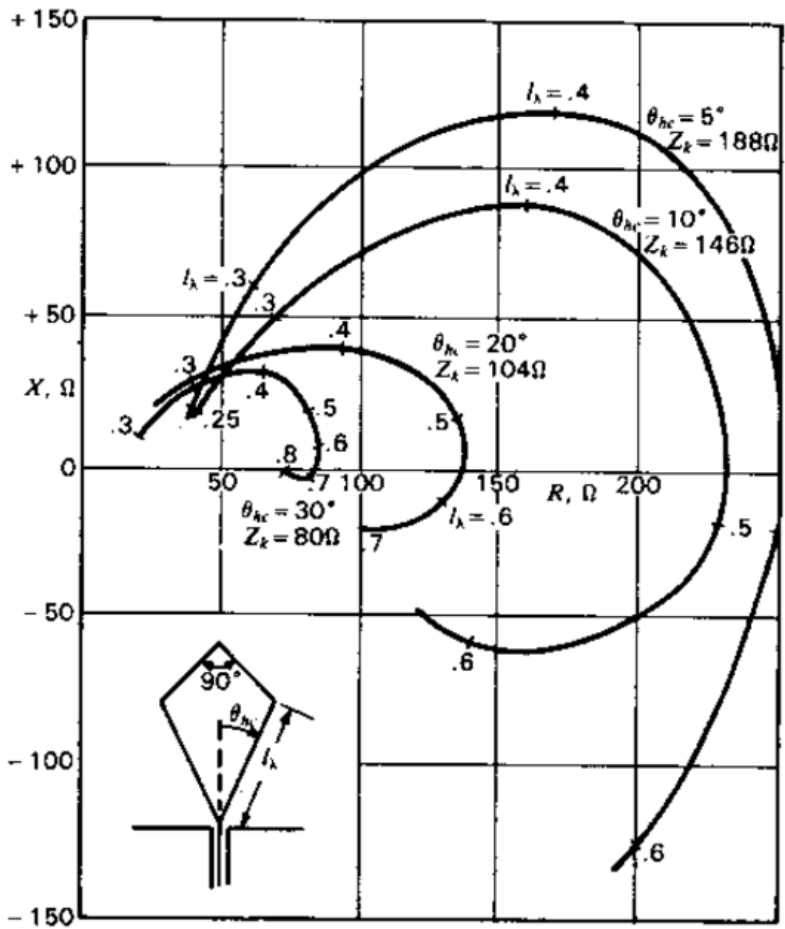


Figure 8-13 Measured input impedance of single cones with top hat as a function of cone length in wavelengths (l_λ). Impedance curves are presented for cones with half-angles of 5, 10, 20 and 30°.

Figure 2.16

2.5.3 Terminator and switch

2.5.4 Low noise amplifier

2.5.5 Signal conditioning

2.5.6 Veto antenna

2.5.7 12 V power system

asdf

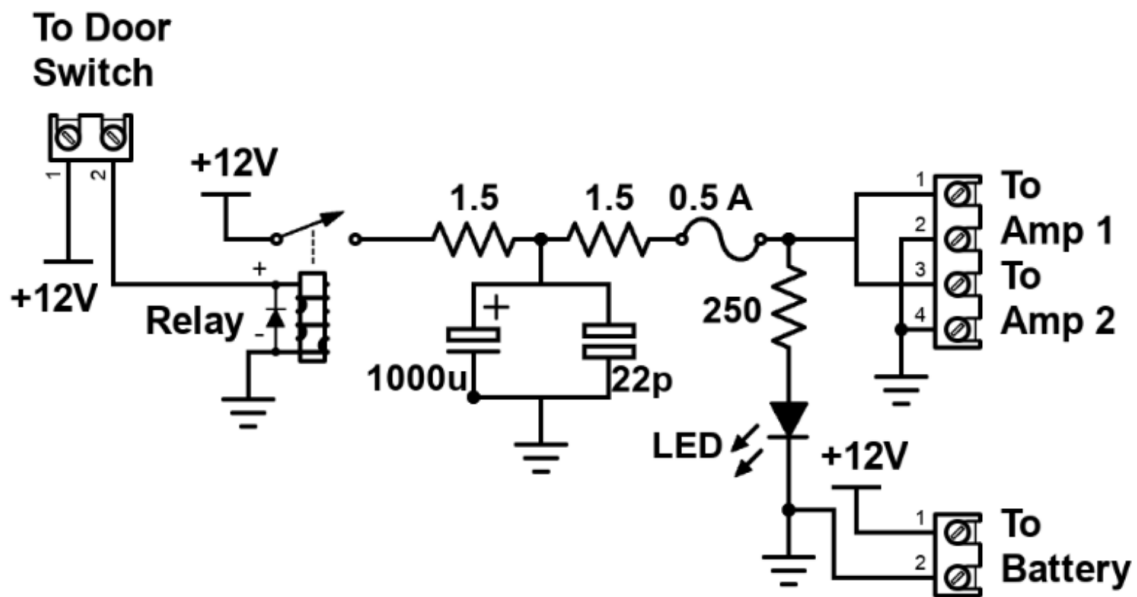


Figure 2.17: Schematic of Interlock board. No voltage regulation is provided because it is designed to work with amplifiers containing internal regulation (Pasternack PE15A1012). Not shown is a simple "slow turn on circuit" consisting of a 0.68 F capacitor and a 8Ω , 10 W resistor (time constant = 5.4 seconds) which was installed to protect the amplifier from transient voltages when the door is closed. Experience has shown the liberal use of fuses to be prudent when working with car batteries in a metal room.

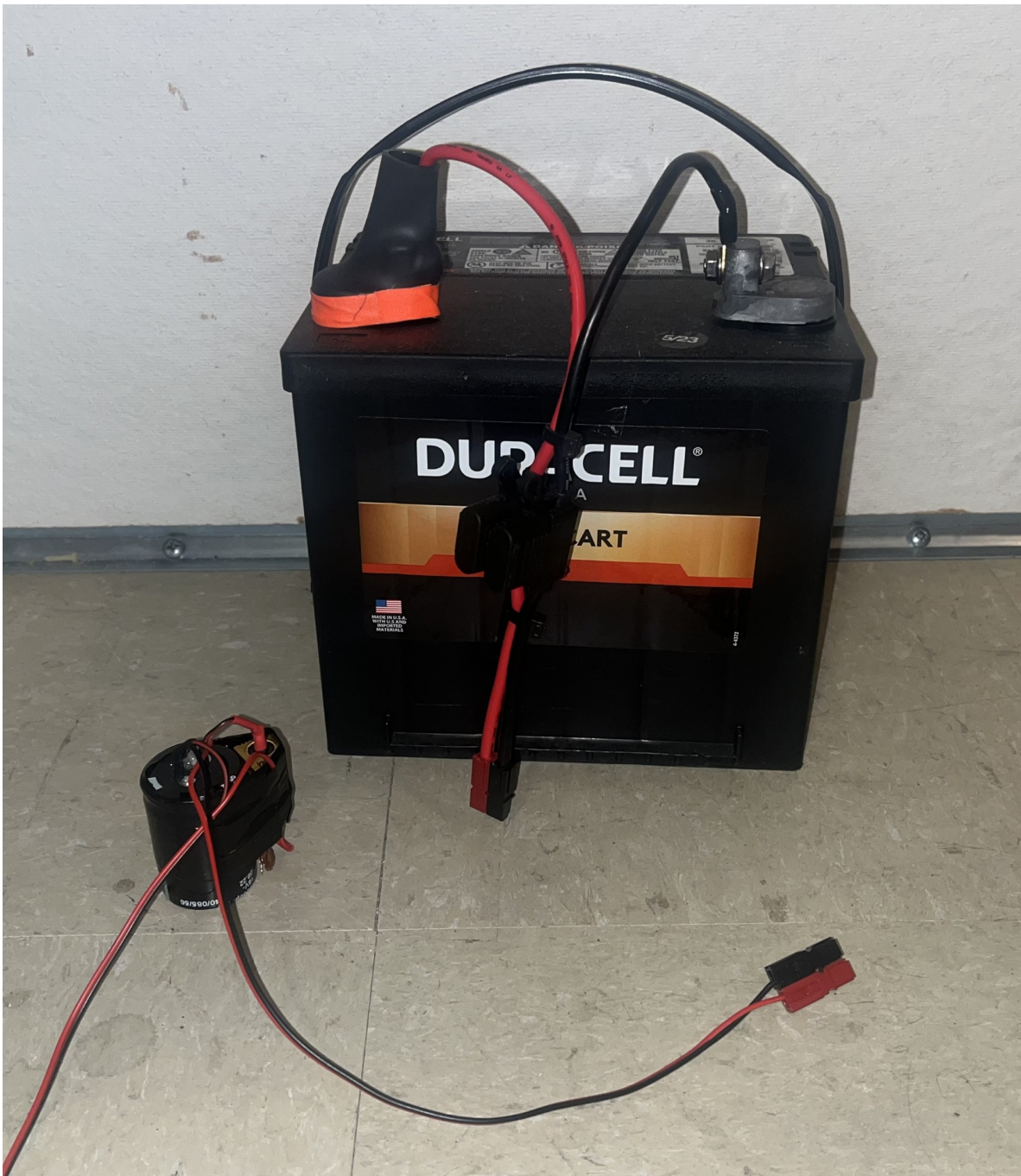


Figure 2.18: Photo of 12V lead-acid battery and slow turn on circuit. Both connect directly to the interlock board shown in Fig. 2.17. Slow turn on circuit is connected between interlock board and amplifier. Battery includes a 2A fast fuse installed in commercial Anderson power pole assembly.

2.5.8 GPU-Based Real-Time Spectrum Analyzer

The use of commercial Spectrum Analyzers (SAs) which feature so called RTSA (real time spectrum analyzer) mode come with several restrictions which limit the efficiency with which they are able to perform wide-band scans with narrow frequency resolution as we point out in our pilot run [**GroupPaper**]. The number of frequency bins output by an discrete Fourier transform (DFT) is equal to the number of time domain samples/2, while the bandwidth is given by sample rate/2. Furthermore, the ability to acquire data in real time requires a DFT algorithm (generally implemented as a fast Fourier transform, FFT) and computation resources which can operate on time domain data at least as fast as it is acquired. From a practical perspective this means that high frequency resolution, wide bandwidth, real time DFTs require modest memory, transfer rates and processing resources. By employing frequency mixers, restrictions on bin counts, and dead time between acquisitions, commercial SAs are able to reduce hardware demands. For this reason we have constructed our own SA based on the Teledyne ADQ32 PCIE digitizer. As a point of reference, the system used in this data run has the specifications outlined in table 2.1. While modest by modern PC standards, these specifications are generally not implemented in commercial SAs.

Bit depth	16 bits
Sample rate	800MHz
DFT input length	2^{24} samples
FFT compute time	2 ms
Channel count	2

Table 2.1: Specifications for the spectrum analyzer used for run 1A.

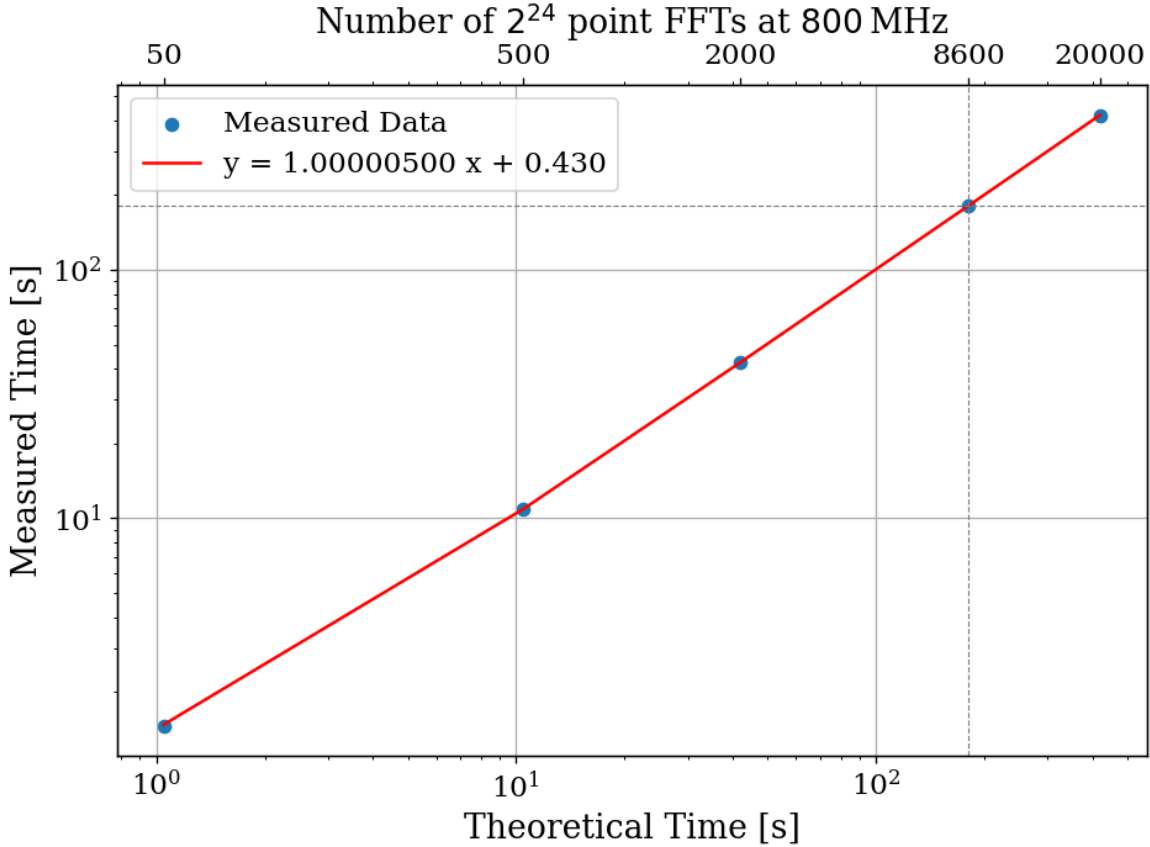


Figure 2.19: Acquisition efficiency for GPU-based Real-time spectrum analyze computed from measured vs theoretical times. The constant offset of 0.43 seconds corresponds to a small set up period when starting an acquisition containing, in the case of run 1A, 8600 FFTs. In the limit of an infinite length acquisition, the system's efficiency can be read off from the slope and is 99.9995%. The more realistic efficiency is a function of number of FFTs per acquisition and for run 1A = 180.3551 [s]/180.7782 [s] = 99.765%.

2.5.9 Spectrum Analyzer Details

After passing through and amplifier and filter chain outlined in section ??, both the main and external antenna signals are digitized by the ADQ32's two ADCs. We utilize a GPU direct write in order to minimize CPU-GPU copies which in our experience tend to be significantly slower than the FFT itself. This GPU direct write is implemented by the digitizer's C++

API. First, several buffers are allocated in GPU memory.

Once written to a pre-allocated, time-domain buffer in the GPU's memory, an FFT is performed using Pytorch which we found to be the fastest across all the GPUs we tested (all Nvidia). [25]

Chapter 3

System Characterization and Data Acquisition

“When you can measure what you are speaking about and express it in numbers you know something about it; but when you cannot measure it, when you cannot express it in numbers your knowledge is of meagre and unsatisfactory kind; it may be the beginning of knowledge but you have scarcely progressed in your thoughts to the stage of science whatever the matter may be.”

- Schematic of experiment
- Detailed schematic of amp chain
- Reason for switching. Cite dickie thermal equilibrium of resistor and antenna in cavity [26]. See 5.9.23 Messing around with different loads in lab book for experiment.

FROM PAPER 1A DRAFT: The dark E-field radio experiment consists of a biconical E-field antenna inside of a cavity. The cavity is implemented as a room temperature commercial shielded room (maufactured by ETS Lindgrin) which serves both to isolate the experiment from external radio frequency interference (RFI) and to provide resonant enhancement of any (coherent?) dark photons after they have converted to standard photons. A low noise amplifier (LNA), secondary amplifier, attenuation and a band pass filter provide analog signal conditioning before the signal is digitized by a GHz ADC (Teledyne ADQ-32), see figure 2.9. From the digitizer, records of length 2^{24} are written to a GPU where a fast Fourier transform (FFT) is performed. Approximately 8000 FFTs are performed and added to a running total on the GPU (representing about 3 minutes of real time data) before dividing by the number of FFTs and copying this averaged spectrum to RAM where it can be saved for future processing, including further averaging. This pre-averaging reduces the ≈ 3 GB/s/channel data stream from the ADC to the GPU down to ≈ 0.3 MB/s/channel which allows for real time copies from the GPU to RAM but comes at the cost of temporal resolution of transient candidates. This is summarized in Fig. 3.1.

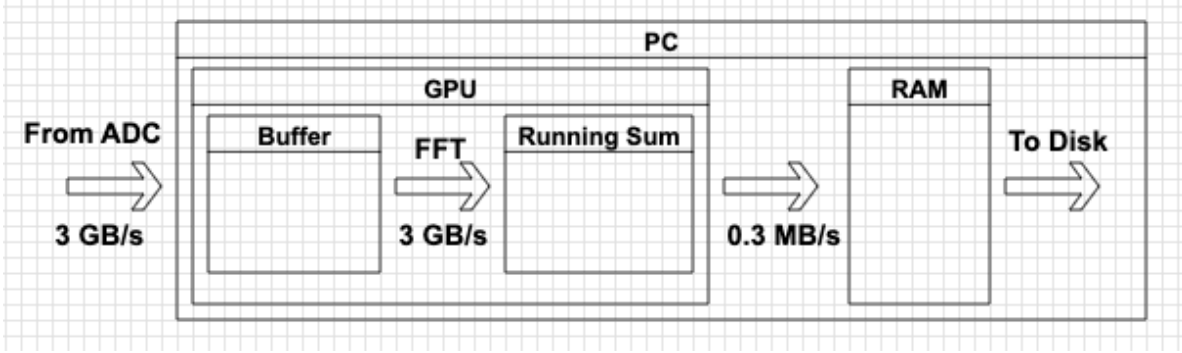


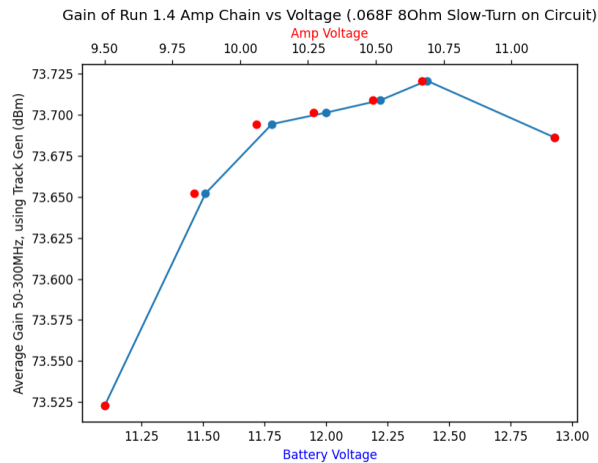
Figure 3.1: Data stream of real time DAQ. This set up is duplicated for channels A and B

3.1 Control and Quantifying of Uncertainties

3.1.1 Direct Measurement of Amp Chain Parameters

- Gain
- Noise schematic

Figure 3.2: Gain vs. voltage of front end amplifier



ADD fig

Chapter 4

Data Analysis and Calibration

We will build up this search in two successive steps. First a basic analysis on the averaged spectrum (roughly equivalent a *processed spectrum* in [haystac[•]2017]) which sets a relatively simple, though conservative limit. The second step accounts for the variation of Q with frequency. This comes into play because a dark photon line with $Q = 1\text{e}6$ would span a single 50 Hz bin at 50 MHz but would span 6 bins at 300MHz. This is accomplished with a signal-matched filter in the frequency domain to improve SNR by compressing the signal's power into as few bins as possible. We observe a small improvement at 50MHz (where the signal is expected to span only a bin or two) and a factor of XXXX improvement at 300MHz, and a linear(JL: check this claim) improvement-factor between these two extremes.

Following an exploration of the details of the analysis pipeline, we take a step back and place the analysis in a black box and perform a Monte Carlo validation of our sensitivity by injecting signals onto a generated background. Our background is white noise riding on a slowly varying undulations and is therefore simple to generate. We employ a simple Monte Carlo method to find the XXXX% confidence limit on power which we would be able to detect. In the absence of a signal, this limit on power can be converted into a limit on epsilon.

4.1 Hardware Injection Test ¹

To validate detection methodology, a separate, proof-of-concept run with an a proxy dark photon signal injected into the shielded room was performed. Apart from the injection

¹Code for this section can be found at: <https://github.com/josephmlev/darkRadio/tree/master/daqAnalysisAndExperiments/run1p4/injectionTesting/injectionTesting.ipynb>

antenna (a 40 cm monopole, see Sec. [add reference: simulation validation](#)), the setup was equivalent to run 1.4, including the data analysis. The proxy dark photon signal (detailed in Sec. 4.1.1.2) was injected at a frequency set by a colleague and was unknown to me at the time of analysis, constituting a “blind” analysis.

4.1.1 Injection test prerequisites

4.1.1.1 Determination of required injected power

comment: S parameters need to be squared. Check on this. See Besnier [27] To accomplish the test, a minimum detectable power required for injection P_{inject} must be computed. P_{inject} should correspond to a signal that can be detected in a predictable amount of time (with some uncertainty, discussed in detail in Sec. [add reference: plot of expected time to detection in toy analysis](#)). A simple way to begin is to read off the detectable, total integrated, power from Fig. [add reference: output referred limit from paper](#). In other words the power contained in a dark photon line, integrated over the few bins spanned by the line ($Q_{\text{DP}} \approx 10^6$, discussed in [add reference: discussion of dp Q, probably ch 1](#)) This gives the amount of output-referred power that would be detectable 95% of the time after 9 days of integration. Since we don’t want to wait 9 days for this test, it is simple to convert this detection limit into one which would be produced in a shorter time by the Dicke radiometer equation, Eq. 2.15. Namely, the limit on power scales like the square root of time², so a one hour integration will require

²It is important to point out that one needs to test whether or not the system in question actually behaves as predicted by the Dicke equation for the amount of averaging in question. After lots of averaging, one may encounter non-thermal backgrounds which do not scale properly. It is shown in [add reference: ch 3 probably](#) that the dark radio system follows the Dicke radiometer equation at least for 9 days. It is also shown for this specific run in Figs. 4.5 and 4.6. **comment:** If you do a simulated spur run/RFI run you can

a factor $\sqrt{9 \text{ days}/1 \text{ hour}} = 14.7$ more power than is shown in [add reference: output referred limit from paper](#).

At this point the simplest way to proceed is to measure the average through power of the monopole to the bicon in several antenna positions $\langle S_{21} \rangle$. This is the same as the set up described in Sec. [add reference: simulation validation, and figure of CAD](#). The bicon was moved to 9 positions and the resulting S parameters were measured at the reference planes shown in Fig. 4.1. They are shown in Fig. 4.2 after being averaged together.

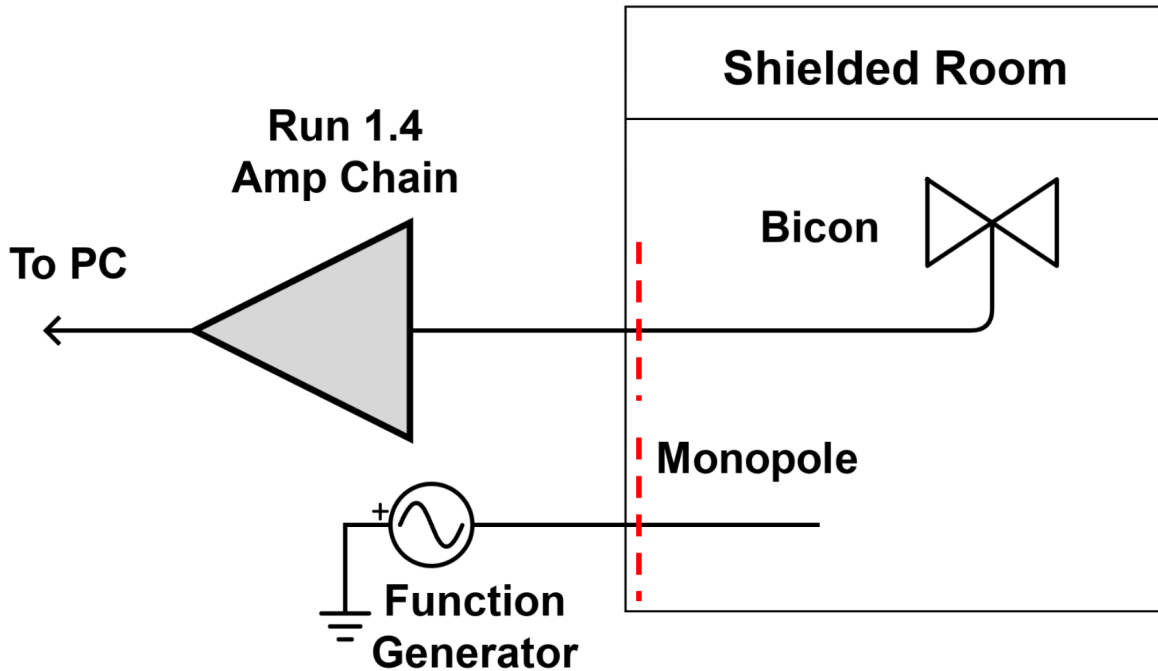


Figure 4.1: Schematic of hardware injection test. Dashed red lines indicate reference planes used to measure S parameters, shown in Fig. 4.2. “Amp Chain” includes everything shown in Fig. [add reference: amp chain schematic, prob ch 2](#)

show it's longer.

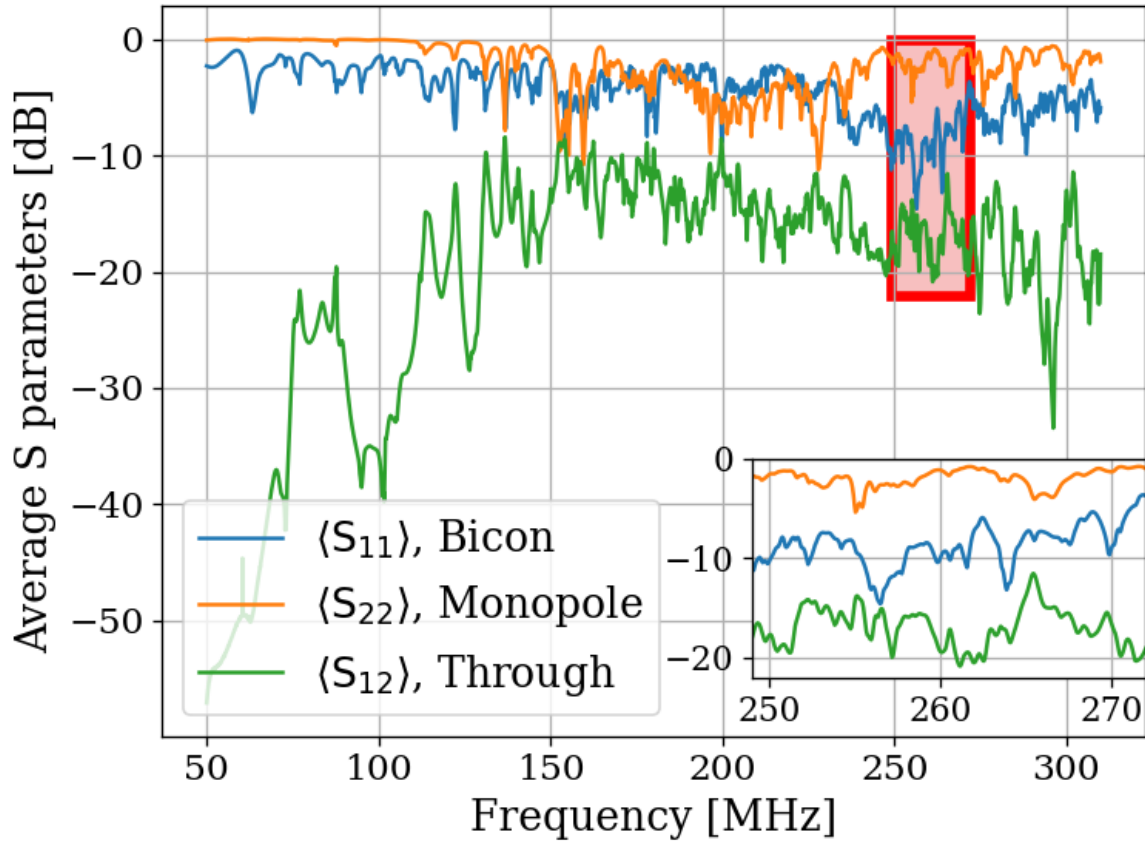


Figure 4.2: Average S parameters of hardware injection test. Taken at 9 positions of the bicon antenna and averaged together (linearly). Ports 1 and 2 are defined to be for the bicon and monopole respectively. Note that $\langle S_{12} \rangle = \langle S_{21} \rangle$ so only $\langle S_{12} \rangle$ is shown. Inset shows zoom on area enclosed by red box.

Knowing the output-referred limit, the system's average S_{21} , and the gain G, allows for a calculation of the required signal strength (as a function of frequency) which will become detectable after a known amount of time. In order to simplify the test, a smaller 1 MHz band is chosen between 268 and 269 MHz for the blind injection, where S_{12} is constant to about 1dB. At first glance, this seems to be cheating, however there are still approximately 21,000 frequency bins in this span, so a detection is very unlikely to be random. Furthermore, the

entire 50-300 MHz span is sent to the detection algorithm (Fig. [add reference: detection alg. from paper](#)) which produces an output without knowing about this frequency restriction.

With all this in mind, the signal power required is simply

$$P_{\text{inject}} = \frac{P_{\text{o}}^{\text{lim}}}{G \langle S_{21} \rangle},$$

where each term is a function of frequency. For the parameters described in this section (including the increase in the power limit $\sqrt{9 \text{ days}/1 \text{ hour}} = 14.7$), this works out to $\approx 6 \times 10^{-19} W$ or -152.5 dBm. The Rigol DSG830 signal generator is not calibrated to such low levels, so this was achieved through attenuation ³.

4.1.1.2 Proxy dark photon signal injection

Now that the power for signal injection has been established, the finite-width proxy-signal ($Q_{\text{DP}} \approx 10^6$) can be generated. An intuitive way to accomplish this would be with an arbitrary waveform generator injecting a time domain signal which is the Fourier transform of the the expected Rayleigh line shape, Eq. 2.23. This is the method of the ADMX experiment (see for example [28]). Another option would be to frequency-modulate a sine wave such that it slowly sweeps out the line shape, spending am amount of time at each frequency weighted by Eq. 2.23. While intuitive, I was unable to get this to work. Zhu et al.'s method of frequency hopping [29] is the discretized version of this and it very simple to implement. The signal generator is set to change frequencies at some interval (discussed below). The frequency which is set is randomly drawn from the PDF of Eq.2.23.

³Experience with this signal generator has shown it exhibits the best performance is when it is set around -30 dBm. Higher than this, large non-harmonic distortions appear contaminating the run. Smaller, and the signal-to-spurious-noise-floor of the generator is poor, also contaminating the run.

There are two considerations that determine the frequency hop period τ_{FH} that the frequency is changed⁴. First, τ_{FH} should be much longer than the acquisition time of a single buffer τ_{FFT} ⁵. On the Rigol signal generator, the power is briefly shut off while the frequency is changed. $\tau_{\text{FFT}} \ll \tau_{\text{FH}}$ ensures that most FFTs of data which don't contain a frequency-hop. Second, τ_{FH} should be small compared to the total time of integration τ , so that there are many frequencies represented in the entire run. In the limiting case, $\tau_{\text{FH}} = \tau$ will yield an averaged spectrum containing a single injected frequency; the proxy-signal will be a delta function in the frequency domain.

Testing has shown that $\tau_{\text{FH}}/\tau_{\text{FFT}} \approx 10$ is more than adequate to address the first consideration. For run 1A (and therefore, this test which shares settings with run 1A), $\tau_{\text{FFT}} = 2^{24}/800$ MHz = 21 ms, so τ_{FH} was set to 250 ms. This means that over 1 hour, the frequency will be set to $\approx 1.4 \times 10^4$, which addresses the second concern. A histogram of this signal is shown in Fig. 4.3.

⁴Zhu et al. randomized this period to prevent any unintentional periodic signals entering. I didn't find this to be necessary.

⁵One can likely bypass this restriction by coordinating the signal generator and ADC such that there is some dead time between collection of buffers, in which the frequency is set. Testing has shown that this restriction is adequate to avoid this extra programming step

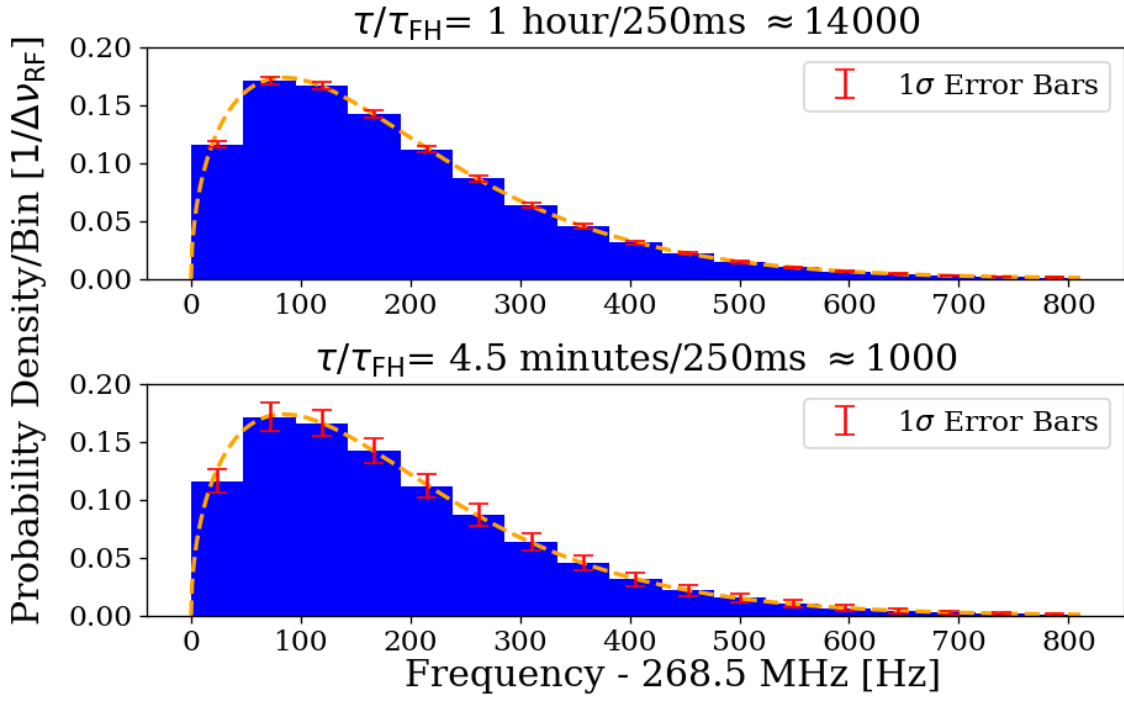


Figure 4.3: Histogram of frequencies used for hardware injection test, with realistic $\Delta\nu_{RF} = 47.7$ Hz. Orange dashed curve is expected line shape from 2.23. Blue histogram and error bars generated from Monte Carlo simulation and shows the mean value per bin, with 1σ error bars in red. This involves generating 1000 lists of random frequencies (each of length τ/τ_{FH}), binning the data and calculating the standard deviation of each bin. τ is the total acquisition time and τ_{FH} is the amount of time spent on each frequency before “hopping” to the next. Their ratio, τ/τ_{FH} is the number of frequencies which are injected in a given injection test, and was approximately 1.4×10^4 for the one hour test outlined in this section. **comment:** There is another version of this plot which has $\tau/\tau_{FH} = 4$ minutes/250ms at the top. I thought I uploaded that

4.1.2 Performing the injection test

Due to the uncertainties involved, more data were taken than the required 1 hour. This also helped produce the pretty plot in Fig. 4 of Levine et al. [add reference: levine et al.](#). 3.6 hours of data were collected, and saved in 30 second pre-averages so that progressively more data could be averaged if the signal was not detected at the predicated time. As mentioned

above, the signal injected was at high frequency so that it would be split up into 5 or 6 bins, testing the matched filter's effectiveness. The bicon was moved to 9 positions. Spectra resulting from 9 antenna positions and 30 seconds of pre-averaging at each position were averaged together giving 4.5 minute time resolution. Three of these spectra are shown in Fig. 4.4. The standard deviation of these spectra average down with the square root of time, closely following the Dicke radiometer equation (discussed in Sec. [add reference: ch 2?](#)). This is shown in Figs. 4.5 and 4.6.

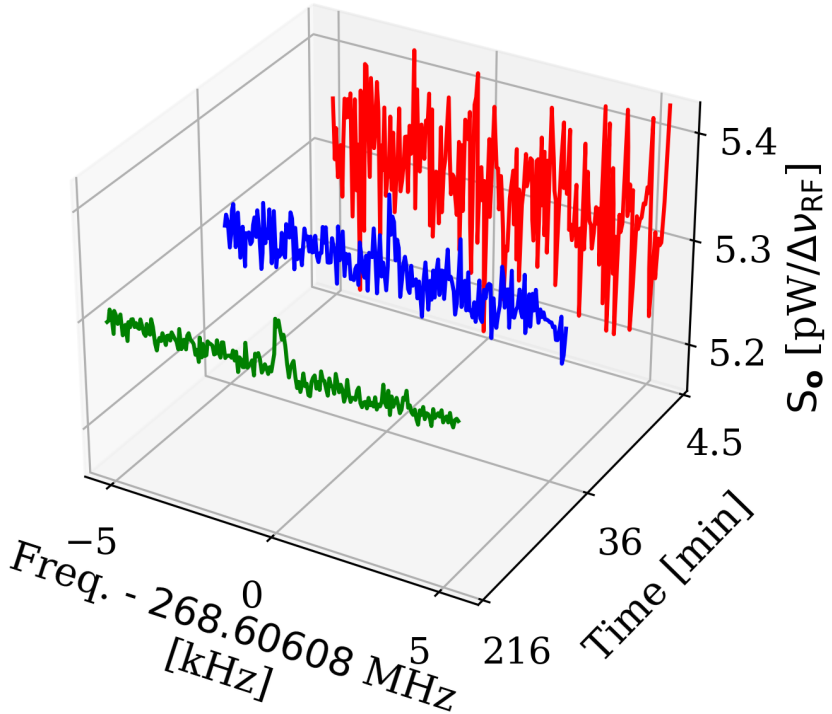


Figure 4.4: Output-referred power spectral density from the hardware injection test illustrating noise averaging down to reveal a persistent, hardware-injected, dark photon proxy signal. Spectra shown are highly zoomed around the injected frequency, 268.60608 MHz. The red, blue and green spectra represent 4.5, 36 and 216 minutes of integration time respectively. The standard deviation of these spectra (excluding the bins containing the injected signal) average down with the square root of time as expected. The blue spectrum shows the amount of averaging required for the signal to be detected by the detection algorithm (including the matched filter) at 5% significance. The tight zoom shown here is less than 1 part in 10^4 of the full 50-300 MHz spectrum analyzed.

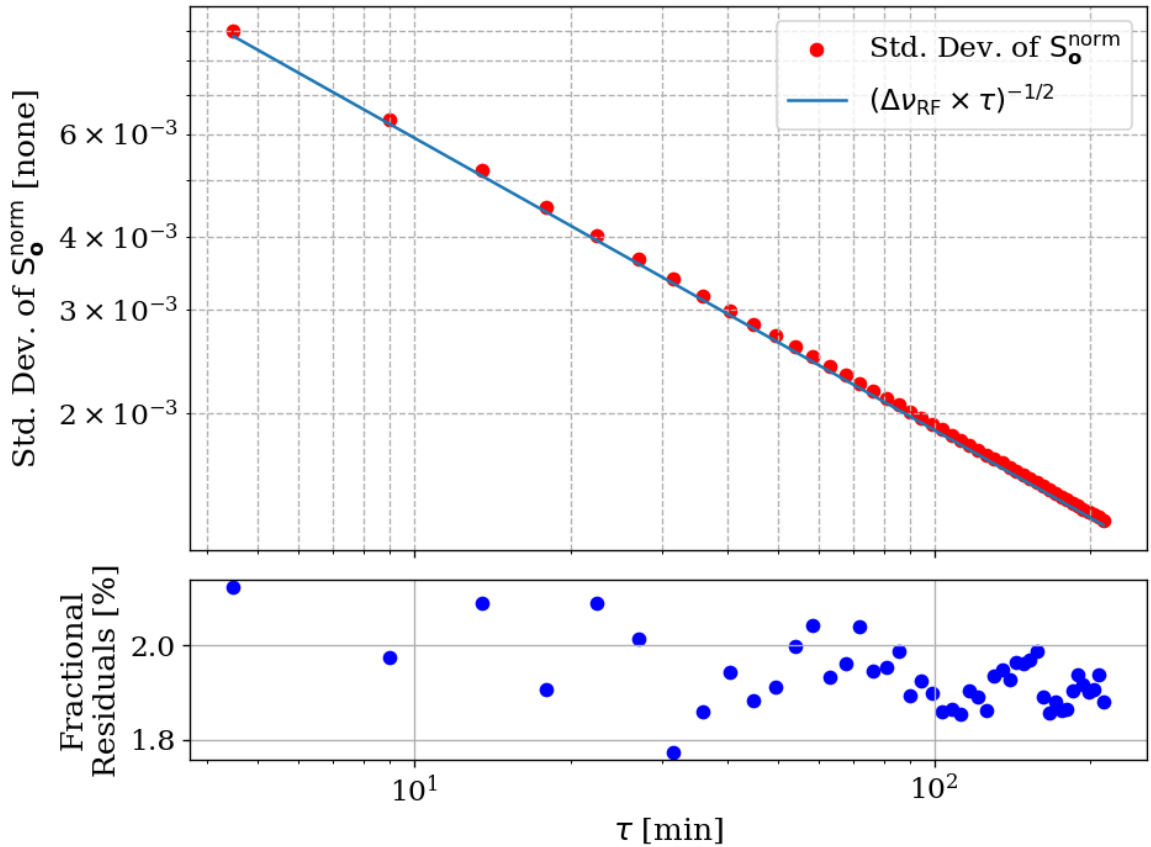


Figure 4.5: Standard deviation of output-referred power spectral density from the hardware injection test. Blue curve is the predicted standard deviation from the Dicke radiometer equation, Eq. 2.15. Each point represents 9 antenna positions with an additional 4.5 minutes of data averaged (see Sec. 4.1.2). Correlation in residuals is expected when computing the standard deviation directly, as outlined in Sec. [Analysis somewhere](#). A better fit is achieved through the median average deviation, Shown in Fig. 4.6.

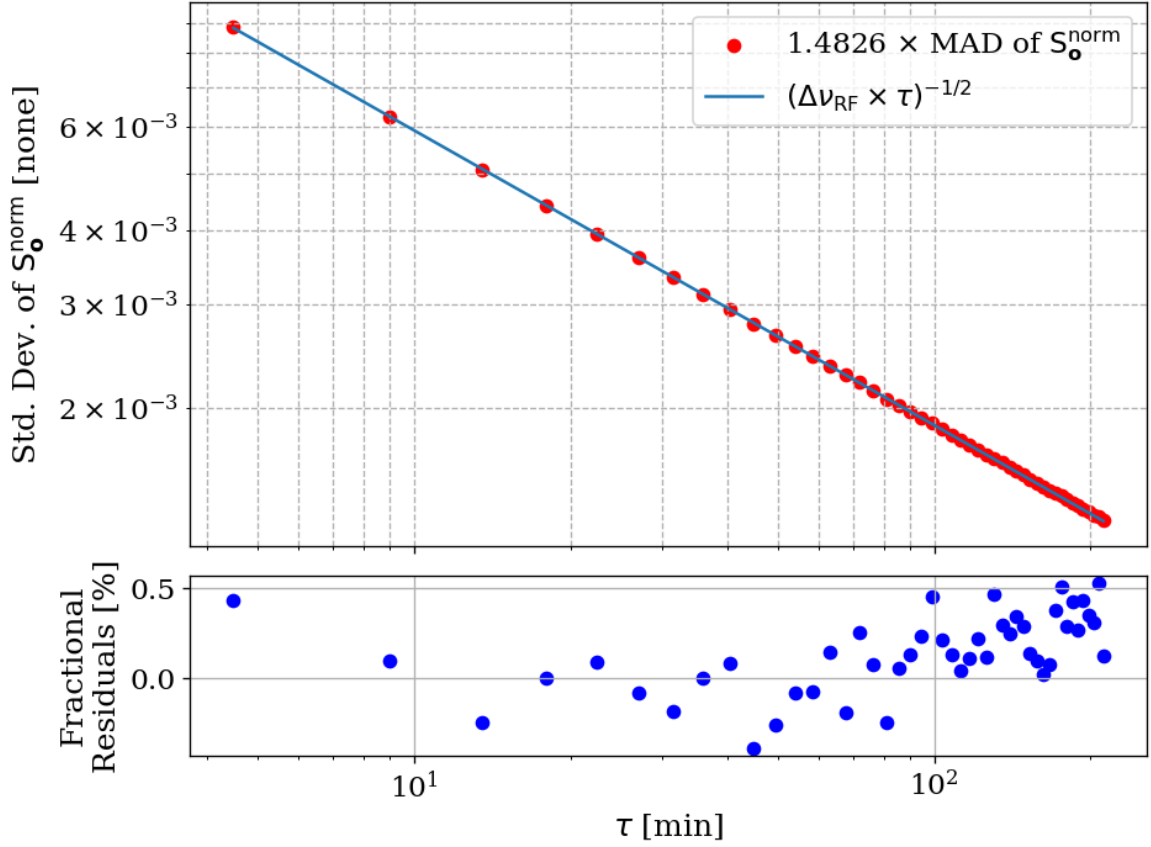


Figure 4.6: Standard deviation of output-referred power spectral density from the hardware injection test, computed with median absolute deviation (MAD). The blue curve represents the predicted standard deviation from the Dicke radiometer equation, Eq. 2.15. Each point corresponds to 9 antenna positions with an additional 4.5 minutes of data averaged (see Sec. 4.1.2). MAD provides a more robust measure of variability, reducing the influence of outliers and offering a better fit than direct standard deviation calculations, as discussed in Sec. [add reference: Analysis somewhere](#).

These spectra were generated one at a time and passed through the detection algorithm described in detail in Sec. [add reference: detection alg](#). The first spectrum where a signal was detected was at 36 minutes, shown in blue in Fig. 4.4. Although hardly detectable to the eye, the matched filter detects the signal with 5% significance. At the point the signal was

detected (i.e. before all data were averaged together), the injection frequency was confirmed to have been correctly identified, resulting in a successful, blind, hardware injection test.

4.1.3 Inspection of Data

This subsection simply contains some full page figures which show data from the injection test. They are all the same 34 minutes of data, but at different stages of processing, closely following [add reference: analysis, earlier in this chapter](#). They are meant to simulate the experience of inspecting a 2^{24} point FFT's power spectrum in a matplotlib widget window. The zoom is seemingly unending, a feature that is difficult to appreciate in a printed document. These figures should provide some context for how futile a manual search of unfiltered data would be.

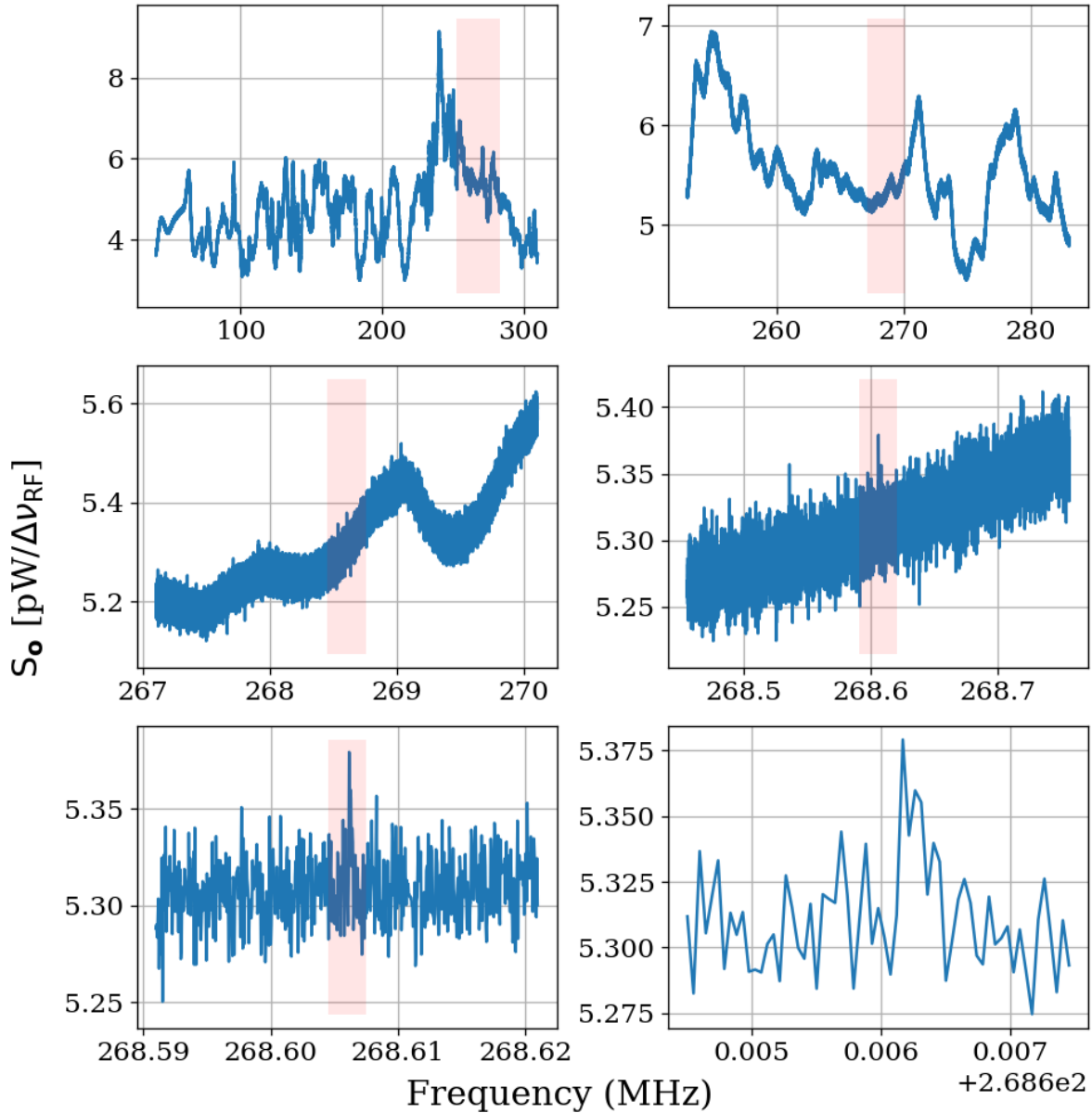


Figure 4.7: Output-referred power spectrum from hardware injection test. Injected signal at 268.60608MHz. All spectra correspond to a total of 36 minuets of averaging, split evenly between 9 antenna positions. Full 50-300 MHz span contains $\approx 5.2 \times 10^6$ bins. Light pink boxes show zoom level on following plot.

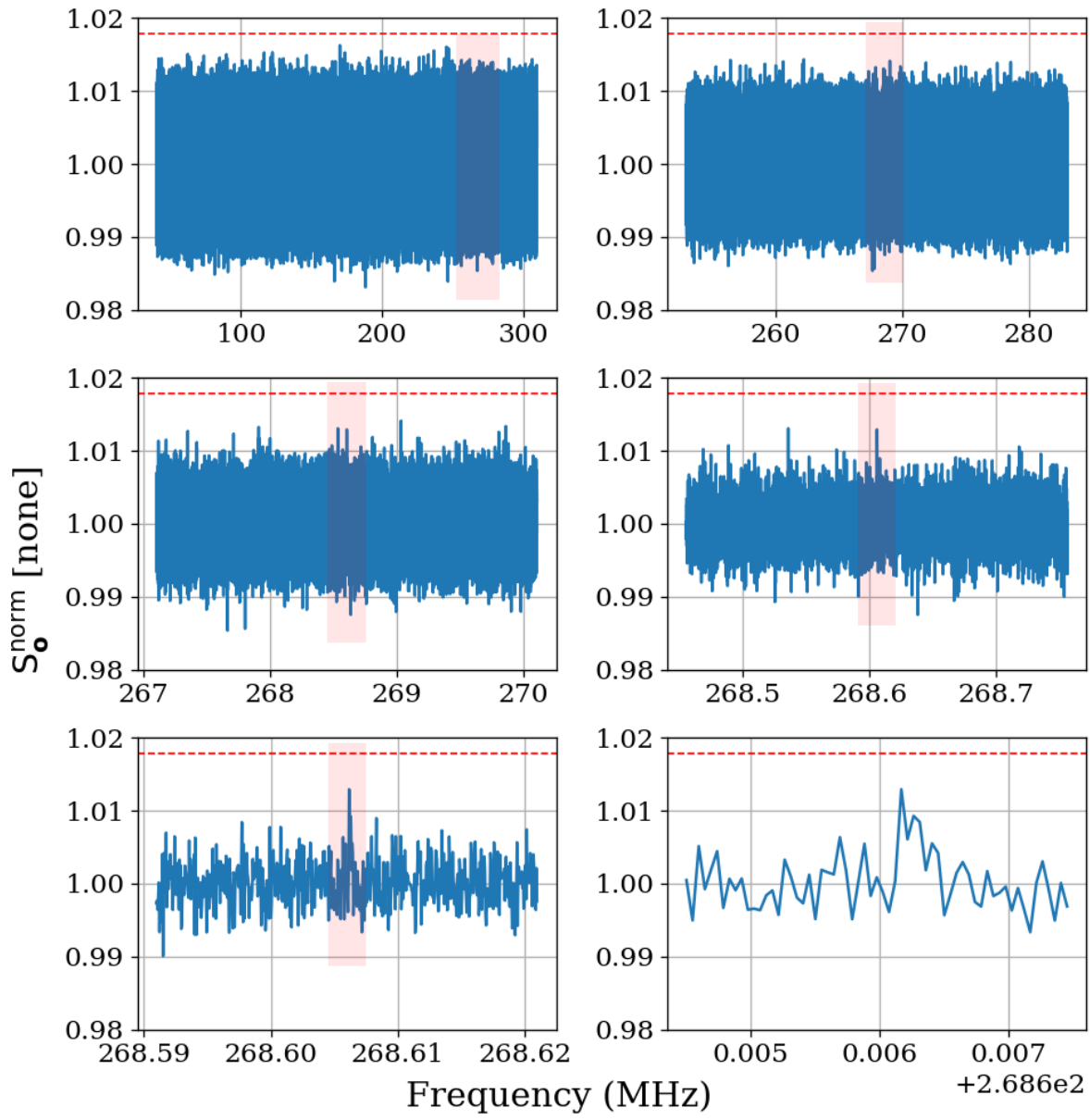


Figure 4.8: Normalized, output-referred power spectrum from hardware injection test. Injected signal at 268.60608MHz. Light pink boxes show zoom level on following plot. Red dashed line indicates the 5% significance threshold (derived in sec [add reference: end of Ch. 2](#)). Signal is not detectable above threshold.

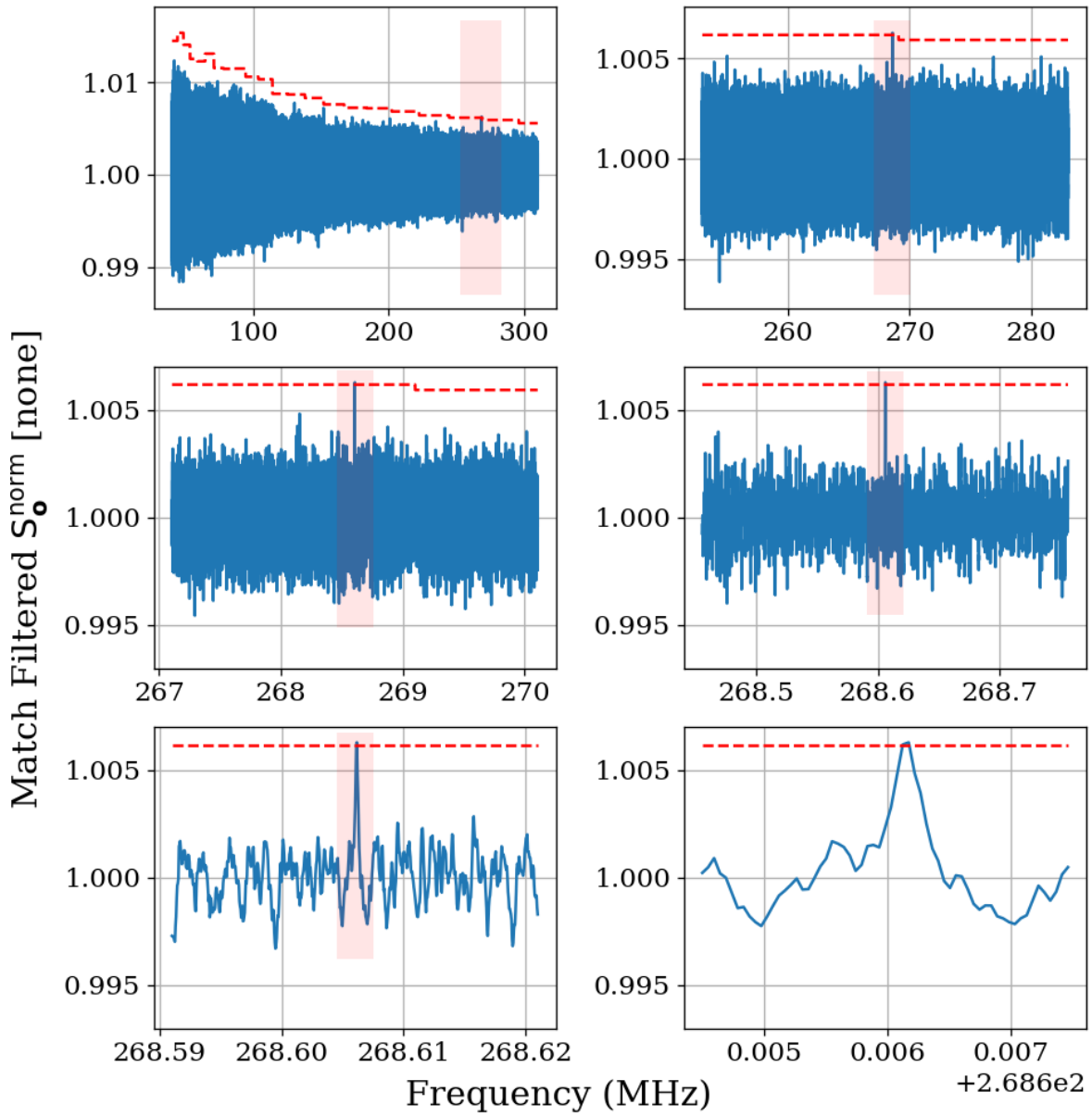


Figure 4.9: Matched filtered, output-referred power spectrum from hardware injection test. Injected signal at 268.60608MHz. Light pink boxes show zoom level on following plot. Red dashed line indicates the 5% significance threshold (derived in sec [add reference: end of Ch. 2](#)). Introducing the matched filter pushed signal above detectable above threshold.

Chapter 5

Beyond 300 MHz

To infinity and beyond!

Buzz Lightyear

Bibliography

- [1] Fritz Zwicky. “The Redshift of Extragalactic Nebulae”. In: (1933).
- [2] Vera C. Rubin and Jr. Ford W. Kent. “Rotation of the Andromeda Nebula from a Spectroscopic Survey of Emission Regions”. In: (1970).
- [3] Marco Battaglieri *et al.* *US Cosmic Visions: New Ideas in Dark Matter 2017: Community Report*. 2017. DOI: 10.48550/ARXIV.1707.04591. URL: <https://arxiv.org/abs/1707.04591>.
- [4] V. Radeka. “Signal, Noise and Resolution in Position-Sensitive Detectors”. In: *IEEE Transactions on Nuclear Science* 21.1 (1974), pp. 51–64. DOI: 10.1109/TNS.1974.4327444.
- [5] David Hill. “Plane Wave Integral Representation for Fields in Reverberation Chambers”. en. In: 40 (1998-08-01 00:08:00 1998).
- [6] W. L. Stutzman and G. A. Thiele. *Antenna Theory and Design*. John Wiley Sons, 1998.
- [7] J.D. Kraus. *Antennas*. McGraw-Hill, 1950. ISBN: 07-035410-3.

- [8] Albert Einstein. “Über die von der molekularkinetischen Theorie der Wärme geforderte Bewegung von in ruhenden Flüssigkeiten suspendierten Teilchen”. In: *Annalen der Physik* 322.8 (1905), pp. 549–560.
- [9] H. Nyquist. “Thermal Agitation of Electric Charge in Conductors”. In: *Phys. Rev.* 32 (1 July 1928), pp. 110–113. DOI: 10.1103/PhysRev.32.110. URL: <https://link.aps.org/doi/10.1103/PhysRev.32.110>.
- [10] Herbert B. Callen and Theodore A. Welton. “Irreversibility and Generalized Noise”. In: *Phys. Rev.* 83 (1 July 1951), pp. 34–40. DOI: 10.1103/PhysRev.83.34. URL: <https://link.aps.org/doi/10.1103/PhysRev.83.34>.
- [11] C. L. Mehta. “Coherence-time and effective bandwidth of blackbody radiation”. In: *Il Nuovo Cimento (1955-1965)* 28.2 (1963), pp. 401–408. DOI: 10.1007/BF02828589. URL: <https://doi.org/10.1007/BF02828589>.
- [12] Raphael Cervantes et al. *Deepest Sensitivity to Wavelike Dark Photon Dark Matter with SRF Cavities*. 2022. arXiv: 2208.03183 [hep-ex].
- [13] Alexander V. Gramolin et al. “Spectral signatures of axionlike dark matter”. In: *Physical Review D* 105.3 (Feb. 2022). ISSN: 2470-0029. DOI: 10.1103/physrevd.105.035029. URL: <http://dx.doi.org/10.1103/PhysRevD.105.035029>.
- [14] Michael S. Turner. “Periodic signatures for the detection of cosmic axions”. In: *Phys. Rev. D* 42 (10 Nov. 1990), pp. 3572–3575. DOI: 10.1103/PhysRevD.42.3572. URL: <https://link.aps.org/doi/10.1103/PhysRevD.42.3572>.

- [15] Greg Durgin. *Lecture on Noise Figure*. Accessed: 2024-06-23. 2017. URL: https://www.youtube.com/watch?v=M_SRUF4TQgA.
- [16] Pasternack Enterprises. *PE15A1012: 1 Watt Amplifier Operating From 0.01 GHz to 6 GHz*. Accessed: 2024-05-17. 2024. URL: <https://www.pasternack.com/images/ProductPDF/PE15A1012.pdf>.
- [17] SP Devices. *ADQ32 Datasheet*. Accessed: 2024-06-23. 2024. URL: https://www.spdevices.com/en-us/Products_/Documents/ADQ32/20-2378%20ADQ32%20datasheet.pdf.
- [18] *Series 83 RF Shielded Enclosure*. Lindgren R.F. Enclosures, Inc. 2021. URL: <https://www.ets-lindgren.com/datasheet/shielding/rf-shielding-and-accessories/11003/1100307>.
- [19] David A. Hill. *Electromagnetic Theory of Reverberation Chambers*. Technical Note 1506. Gaithersburg, MD: National Institute of Standards and Technology, 1998. URL: https://tsapps.nist.gov/publication/get_pdf.cfm?pub_id=24427.
- [20] D.A. Hill. “A reflection coefficient derivation for the Q of a reverberation chamber”. In: *IEEE Transactions on Electromagnetic Compatibility* 38.4 (1996), pp. 591–592. DOI: 10.1109/15.544314.
- [21] Lawrence Krauss et al. “Calculations for cosmic axion detection”. In: *Physical Review Letters* 55.17 (1985), pp. 1797–1800. DOI: 10.1103/PhysRevLett.55.1797. URL: <https://doi.org/10.1103/PhysRevLett.55.1797>.

- [22] “IEEE Standard Method for Measuring the Effectiveness of Electromagnetic Shielding Enclosures”. In: *IEEE Std 299-1997* (1998), pp. 1–48. DOI: 10.1109/IEEESTD.1998.88115.
- [23] *Biconical Antenna AB-900A*. Rev. D05.19. Com-Power Corporation. May 2019. URL: <https://documentation.com-power.com/pdf/AB-900A-1.pdf>.
- [24] John D. Kraus. *Antennas*. 2nd. New York: McGraw-Hill, 1988, p. 892. ISBN: 9780070354227.
- [25] CuPy Developers. *CuPy: NumPy-compatible array library accelerating machine learning with CUDA*. https://docs.cupy.dev/en/stable/user_guide/interoperability.html. Accessed on: May 11, 2023. 2021.
- [26] Robert H Dicke. “The measurement of thermal radiation at microwave frequencies”. In: *Review of Scientific Instruments* 17.7 (1946), pp. 268–275.
- [27] Philippe Besnier, Christophe Lemoine, and Jerome Sol. “Various estimations of composite Q-factor with antennas in a reverberation chamber”. In: *2015 IEEE International Symposium on Electromagnetic Compatibility (EMC)*. 2015, pp. 1223–1227. DOI: 10.1109/ISEMC.2015.7256344.
- [28] R. Khatiwada et al. “Axion Dark Matter Experiment: Detailed design and operations”. In: *Review of Scientific Instruments* 92.12 (Dec. 2021), p. 124502. ISSN: 0034-6748. DOI: 10.1063/5.0037857. eprint: <https://pubs.aip.org/aip/rsi/article-pdf/doi/10.1063/5.0037857/16136265/124502\1\online.pdf>. URL: <https://doi.org/10.1063/5.0037857>.

- [29] Yuqi Zhu et al. “An improved synthetic signal injection routine for the Haloscope At Yale Sensitive To Axion Cold dark matter (HAYSTAC)”. In: *Review of Scientific Instruments* 94.5 (May 2023). ISSN: 1089-7623. DOI: 10.1063/5.0137870. URL: <http://dx.doi.org/10.1063/5.0137870>.